UNIVERSITY OF AMSTERDAM

UvA-DARE (Digital Academic Repository)

A JWST Survey of the Supernova Remnant Cassiopeia A

Milisavljevic, D.; Temim, T.; De Looze, I.; Dickinson, D.; Laming, J.M.; Fesen, R.; Raymond, J.C.; Arendt, R.G.; Vink, J.; Posselt, B.; Pavlov, G.G.; Fox, O.D.; Pinarski, E.; Subrayan, B.; Schmidt, J.; Blair, W.P.; Rest, A.; Patnaude, D.; Koo, B.-C.; Rho, J.; Orlando, S.; Janka, H.-T.; Andrews, M.; Barlow, M.J.; Burrows, A.; Chevalier, R.; Clayton, G.; Fransson, C.; Fryer, C.; Gomez, H.L.; Kirchschlager, F.; Lee, J.-J.; Matsuura, M.; Niculescu-Duvaz, M.; Pierel, J.D.R.; Plucinsky, P.P.; Priestley, F.D.; Ravi, A.P.; Sartorio, N.S.; Schmidt, F.; Shahbandeh, M.; Slane, P.; Smith, N.; Sravan, N.; Weil, K.; Wesson, R.; Wheeler, J.C.

DOI
10.3847/2041-8213/ad324b

Publication date
2024

Document Version
Final published version

Published in
Astrophysical Journal Letters

License
CC BY

Link to publication

Citation for published version (APA):
Milisavljevic, D., Temim, T., De Looze, I., Dickinson, D., Laming, J. M., Fesen, R., Raymond, J. C., Arendt, R. G., Vink, J., Posselt, B., Pavlov, G. G., Fox, O. D., Pinarski, E., Subrayan, B., Schmidt, J., Blair, W. P., Rest, A., Patnaude, D., Koo, B.-C., ... Wheeler, J. C. (2024). A JWST Survey of the Supernova Remnant Cassiopeia A. *Astrophysical Journal Letters*, *965*(2), Article L27. https://doi.org/10.3847/2041-8213/ad324b

General rights
It is not permitted to download or to forward/distribute the text or part of it without the consent of the author(s) and/or copyright holder(s), other than for strictly personal, individual use, unless the work is under an open content license (like Creative Commons).

UvA-DARE is a service provided by the library of the University of Amsterdam (https://dare.uva.nl)

Disclaimer/Complaints regulations
If you believe that digital publication of certain material infringes any of your rights or (privacy) interests, please let the Library know, stating your reasons. In case of a legitimate complaint, the Library will make the material inaccessible and/or remove it from the website. Please Ask the Library: https://uba.uva.nl/en/contact, or a letter to: Library of the University of Amsterdam, Secretariat, P.O. Box 19185, 1000 GD Amsterdam, The Netherlands. You will be contacted as soon as possible.

Download date:12 10月 2026

The Astrophysical Journal Letters, 965:L27 (21pp), 2024 April 20 https://doi.org/10.3847/2041-8213/ad324b
© 2024. The Author(s). Published by the American Astronomical Society.
OPEN ACCESS

A JWST Survey of the Supernova Remnant Cassiopeia A

Dan Milisavljevic[1,2], Tea Temim[3], Ilse De Looze[4], Danielle Dickinson[1], J. Martin Laming[5], Robert Fesen[6], John C. Raymond[7], Richard G. Arendt[8,9,10], Jacco Vink[11,12], Bettina Posselt[13,14], George G. Pavlov[14], Ori D. Fox[15], Ethan Pinarski[1], Bhagya Subrayan[1], Judy Schmidt[16], William P. Blair[17], Armin Rest[15,17], Daniel Patnaude[7], Bon-Chul Koo[18], Jeonghee Rho[19,20], Salvatore Orlando[21], Hans-Thomas Janka[22], Moira Andrews[1], Michael J. Barlow[23], Adam Burrows[3], Roger Chevalier[24], Geoffrey Clayton[25], Claes Fransson[26], Christopher Fryer[27,28,29,30], Haley L. Gomez[31], Florian Kirchschlager[4], Jae-Joon Lee[32], Mikako Matsuura[31], Maria Niculescu-Duvaz[23], Justin D. R. Pierel[15], Paul P. Plucinsky[7], Felix D. Priestley[31], Aravind P. Ravi[33], Nina S. Sartorio[4], Franziska Schmidt[23], Melissa Shahbandeh[15], Patrick Slane[7], Nathan Smith[34], Niharika Sravan[35], Kathryn Weil[1], Roger Wesson[31], and J. Craig Wheeler[36]

[1] Purdue University, Department of Physics and Astronomy, 525 Northwestern Avenue, West Lafayette, IN 47907, USA
[2] Integrative Data Science Initiative, Purdue University, West Lafayette, IN 47907, USA
[3] Princeton University, 4 Ivy Lane, Princeton, NJ 08544, USA
[4] Sterrenkundig Observatorium, Ghent University, Krijgslaan 281—S9, B-9000 Gent, Belgium
[5] Space Science Division, Code 7684, Naval Research Laboratory, Washington, DC 20375, USA
[6] 6127 Wilder Lab, Department of Physics and Astronomy, Dartmouth College, Hanover, NH 03755, USA
[7] Center for Astrophysics, Harvard & Smithsonian, 60 Garden Street, Cambridge, MA 02138, USA
[8] Center for Space Sciences and Technology, University of Maryland, Baltimore County, Baltimore, MD 21250, USA
[9] Code 665, NASA/GSFC, 8800 Greenbelt Road, Greenbelt, MD 20771, USA
[10] Center for Research and Exploration in Space Science and Technology, NASA/GSFC, Greenbelt, MD 20771, USA
[11] Anton Pannekoek Institute for Astronomy & GRAPPA, University of Amsterdam, Science Park 904, 1098 XH Amsterdam, The Netherlands
[12] SRON Netherlands Institute for Space Research, Niels Bohrweg 4, 2333 CA Leiden, The Netherlands
[13] Department of Astrophysics, University of Oxford, Denys Wilkinson Building, Keble Road, Oxford OX1 3RH, UK
[14] Department of Astronomy & Astrophysics, Pennsylvania State University, 525 Davey Lab, University Park, PA 16802, USA
[15] Space Telescope Science Institute, 3700 San Martin Drive, Baltimore, MD 21218, USA
[16] Astrophysics Source Code Library, Michigan Technological University, 1400 Townsend Drive, Houghton, MI 49931, USA
[17] The William H. Miller III Department of Physics and Astronomy, Johns Hopkins University, 3400 North Charles Street, Baltimore, MD 21218, USA
[18] Department of Physics and Astronomy, Seoul National University, Seoul 08861, Republic of Korea
[19] SETI Institute, 189 Bernardo Avenue, Suite 200, Mountain View, CA 94043, USA
[20] Department of Physics and Astronomy, Seoul National University, Gwanak-ro 1, Gwanak-gu, South Seoul, 08826, Republic of Korea
[21] INAF—Osservatorio Astronomico di Palermo, Piazza del Parlamento 1, 90134 Palermo, Italy
[22] Max-Planck-Institut für Astrophysik, Karl-Schwarzschild-Str. 1, 85748, Garching, Germany
[23] Department of Physics and Astronomy, University College London, Gower Street, London WC1E 6BT, UK
[24] Department of Astronomy, University of Virginia, P.O. Box 400325, Charlottesville, VA 22904-4325, USA
[25] Department of Physics and Astronomy, Louisiana State University, Baton Rouge, LA 70803, USA
[26] Department of Astronomy, Stockholm University, The Oskar Klein Centre, AlbaNova, SE-106 91 Stockholm, Sweden
[27] Center for Theoretical Astrophysics, Los Alamos National Laboratory, Los Alamos, NM 87545, USA
[28] Department of Astronomy, The University of Arizona, Tucson, AZ 85721, USA
[29] Department of Physics and Astronomy, The University of New Mexico, Albuquerque, NM 87131, USA
[30] Department of Physics, The George Washington University, Washington, DC 20052, USA
[31] Cardiff Hub for Astrophysical Research and Technology (CHART), School of Physics & Astronomy, Cardiff University, The Parade, Cardiff CF24 3AA, UK
[32] Korea Astronomy and Space Science Institute, Daejeon 305-348, Republic of Korea
[33] Department of Physics and Astronomy, University of California, 1 Shields Avenue, Davis, CA 95616-5270, USA
[34] Steward Observatory, University of Arizona, 933 North Cherry Avenue, Tucson, AZ 85721, USA
[35] Department of Physics, Drexel University, Philadelphia, PA 19104, USA
[36] Department of Astronomy, University of Texas at Austin, Austin, TX, USA
Received 2023 December 22; revised 2024 March 6; accepted 2024 March 10; published 2024 April 16

Abstract

We present initial results from a James Webb Space Telescope (JWST) survey of the youngest Galactic core-collapse supernova remnant, Cassiopeia A (Cas A), made up of NIRCam and MIRI imaging mosaics that map emission from the main shell, interior, and surrounding circumstellar/interstellar material (CSM/ISM). We also present four exploratory positions of MIRI Medium Resolution Spectrograph integral field unit spectroscopy that sample ejecta, CSM, and associated dust from representative shocked and unshocked regions. Surprising discoveries include (1) a weblike network of unshocked ejecta filaments resolved to ∼0.01 pc scales exhibiting an overall morphology consistent with turbulent mixing of cool, low-entropy matter from the progenitor's oxygen layer with hot, high-entropy matter heated by neutrino interactions and radioactivity; (2) a thick sheet of dust-dominated emission from shocked CSM seen in projection toward the remnant's interior pockmarked with small (∼1″) round holes formed by $\lesssim$0.″1 knots of high-velocity ejecta that have pierced through the CSM and driven expanding tangential shocks; and (3) dozens of light echoes with angular sizes between ∼0.″1 and 1′ reflecting

Original content from this work may be used under the terms of the Creative Commons Attribution 4.0 licence. Any further distribution of this work must maintain attribution to the author(s) and the title of the work, journal citation and DOI.

previously unseen fine-scale structure in the ISM. NIRCam observations place new upper limits on infrared emission ($\lesssim$20 nJy at 3 μm) from the neutron star in Cas A's center and tightly constrain scenarios involving a possible fallback disk. These JWST survey data and initial findings help address unresolved questions about massive star explosions that have broad implications for the formation and evolution of stellar populations, the metal and dust enrichment of galaxies, and the origin of compact remnant objects.

Unified Astronomy Thesaurus concepts: Core-collapse supernovae (304); Supernova remnants (1667); Neutron stars (1108)

1. Introduction

Core-collapse supernovae (SNe) are among the most consequential phenomena in the Universe, and yet many key questions about their explosion mechanisms and progenitor systems remain unanswered (see, e.g., Smartt 2009 and Janka 2012; Eldridge et al. 2013 and Burrows & Vartanyan 2021). This uncertainty in our understanding has broad and important implications: SNe collectively shape the energy balance, chemistry, and structure of galaxies (Dalla Vecchia & Schaye 2008); they produce neutron stars (NSs), black holes, and some gamma-ray bursts (Woosley et al. 2002); they are a major site of nucleosynthesis (Nomoto et al. 2013), dust production (Hoyle & Wickramasinghe 1970), and cosmic rays (Blasi 2013); and they produce neutrinos (Hirata et al. 1987; Al Kharusi et al. 2021) and gravitational waves (Murphy et al. 2009; Andresen et al. 2017) that can now be studied with multimessenger facilities (Szczepańczyk et al. 2021; Vartanyan et al. 2023).

The superior resolution and sensitivity to near-infrared (NIR) and mid-infrared wavelengths made possible with the successful launch of the James Webb Space Telescope (JWST; Gardner et al. 2023) has opened new pathways to investigate fundamental questions about the nature of SNe via observations of young SN remnants (SNRs). While recent and upcoming all-sky surveys (Tonry et al. 2018; Bellm et al. 2019; Ivezić et al. 2019) can find tens of thousands of extragalactic SNe, analyses of these unresolved events face unavoidable limitations due to their inability to provide clear and robust 3D kinematic and chemical information. In contrast, access to many of the specific and detailed properties needed to advance our understanding of massive star explosions can only be obtained through spatially resolved observations of young ($\lesssim$2000 yr) Galactic SNRs (Milisavljevic & Fesen 2017).

The NIR-to-mid-infrared spectral region uniquely accesses emission from cool, unshocked SN debris, which enables unique insight into the total mass, relative chemical yield, and kinematic distribution of various components of the SN ejecta (Laming & Temim 2020). It also enables investigations about how much ejecta is transformed into dust and how much of that dust survives passage through the reverse shock (Bianchi & Schneider 2007; Dwek & Arendt 2008; Williams & Temim 2017; Priestley et al. 2021). Finally, the infrared region also avoids much of the problem with foreground extinction toward Galactic remnants, providing new opportunities to constrain the processes governing the formation and final fate of compact objects made in SN explosions (De Luca 2017).

Cassiopeia A (Cas A) is arguably the SNR that provides the clearest access to the properties of a core-collapse SN (Koo & Park 2017). Cas A is the youngest Galactic core-collapse SNR known ($\approx$350 yr; Fesen et al. 2006a), it is among the closest ($3.4^{+0.3}_{-0.1}$ kpc; Reed et al. 1995; Alarie et al. 2014), it is the only core-collapse remnant with a secure SN classification from light-echo spectroscopy performed from multiple lines of sight (Type IIb; Krause et al. 2008; Rest et al. 2008, 2011), it is one of the best case studies to understand dust formation in SN ejecta and shock processing of that dust (Rho et al. 2009; De Looze et al. 2017), and its central X-ray point source is a key object to understanding NS evolution models (Pavlov & Luna 2009; Gotthelf et al. 2013; Posselt & Pavlov 2022; Shternin et al. 2023). Models for the remnant suggest that the 15–25 $M_{\odot}$ zero-age main-sequence progenitor star lost the majority of its mass prior to explosion as a $\approx$4–6 $M_{\odot}$ star (Chevalier & Oishi 2003; Hwang & Laming 2012; Lee et al. 2014), which was likely encouraged through interaction with a binary companion (Young et al. 2006; Sato et al. 2020). Although claims have been made of surviving OB companions in extragalactic SNe IIb (Maund et al. 2004; Ryder et al. 2018), Hubble Space Telescope (HST) observations have ruled out this possibility for Cas A, and to date, no surviving companion has been located (Kochanek 2018; Kerzendorf et al. 2019).

Here we present an overview of a JWST reconnaissance of Cas A made up of NIR and mid-infrared imaging mosaics and exploratory spectroscopy. This survey was motivated by outstanding questions about the nature of Cas A's progenitor system, the explosion dynamics of the original SN, and the processes influencing the formation and destruction of dust and molecules. These topics are relevant for broader populations of SNe and their environmental impacts, which in turn have consequences for the formation and evolution of stellar populations (Eldridge et al. 2008; Smith 2014), the metal enrichment of galaxies (Vogelsberger et al. 2014; Nelson et al. 2019), and the origin of planetary systems (Dwek 1998; Nittler & Ciesla 2016).

Our NIRCam, MIRI, and MIRI Medium Resolution Spectrograph (MRS) observations are described in Section 2, followed by Sections 3 and 4, where we present the imaging mosaics and integral field unit (IFU) spectra and highlight the data quality and our major findings with regard to mapping dust and unshocked interior ejecta. We then discuss the serendipitous discovery of a large, bright light echo that resolves the surrounding interstellar material (ISM) in Section 5 and compare our JWST data to radio and X-ray observations in Section 6. The use of the NIRCam images to constrain possible infrared emission from the surviving NS is discussed in Section 7, and we review the major findings and describe new science opportunities enabled by our survey in Section 8.

2. Observations

Cas A was observed with JWST in Cycle 1 General Observers (GO) Program 1947 (PI: Milisavljevic). The observations reported here were carried out between 2022 August and November using NIRCam (Rieke et al. 2023) and MIRI (Wright et al. 2023). NIRSpec (Jakobsen et al. 2022) observations obtained as part of this program that overlap with the MIRI/MRS positions are reported in I. De Looze et al.

Table 1
Image Mosaics Obtained in the Survey

Instrument	Filter	λ_p (μm)	BW (μm)	PSF (arcsec)	t_{exp} (s)	Date (UT)	Sources of Strong Emission
NIRCam	F162M	1.626	0.168	0.055	3350	2022 Nov 5	[Fe II] 1.644; [Si I] 1.645; synchrotron
	F356W	3.563	0.787	0.116	1675	2022 Nov 5	[Ca IV] 3.207; [Si IX] 3.936; PAHs; synchrotron; dust
	F444W	4.421	1.024	0.145	1675	2022 Nov 5	[Si IX] 3.936; [Ca V] 4.159; [Mg IV] 4.487; [Ar VI] 4.530; [K III] 4.618; CO; synchrotron; dust
MIRI	F560W	5.6	1.2	0.207	1598	2022 Aug 4–5, Oct 22	[Mg V] 5.61; dust; synchrotron
	F770W	7.7	2.2	0.269	1598	2022 Aug 4–5, Oct 22	[Ar II] 6.99; PAHs; dust
	F1000W	10.0	2.0	0.328	1598	2022 Aug 4–5, Oct 22	[Ar III] 8.991; [S IV] 10.511; dust
	F1130W	11.3	0.7	0.375	1598	2022 Aug 4–5, Oct 22	PAHs; dust
	F1280W	12.8	2.4	0.420	1598	2022 Aug 4–5, Oct 22	[Ne II] 12.814; [Ne V] 14.32; dust
	F1800W	18.0	3.0	0.591	1598	2022 Aug 4–5, Oct 22	[Fe II] 17.94; [S III] 18.713; dust; H_2
	F2100W	21.0	5.0	0.674	1598	2022 Aug 4–5, Oct 22	[S III] 18.713; dust
	F2550W	25.5	4.0	0.803	1598	2022 Aug 4–5, Oct 22	[O IV] 25.89; dust

Note. Values for filter pivot wavelength (λ_p), bandwidth (BW), and FWHM of the PSF have been adopted from JWST User Documentation (https://jwst-docs.stsci.edu/). t_{exp} is the total exposure time for the mosaic. Line identifications guided in part by Smith et al. (2009) and Laming & Temim (2020).

(2024, in preparation) and Rho et al. (2024). All JWST data used in this paper can be found in MAST: 10.17909/szf2-bg42.

The NIRCam observations were obtained on 2022 November 5 using three filters, as shown in Table 1. The F162M filter was repeated in the Short Wavelength (SW) camera during both of the Long Wavelength (LW) camera exposures using filters F356W and F444W. The remnant was covered using a 3×1 mosaic with 3TIGHT primary dithers, each with 4 subpixel dithers. The field center is approximately α(J2000.0) = 23:23:23.91, δ(J2000.0) = +58:48:54.0, with the entire field of view (FOV) spanning approximately $6.'3 \times 7'$ and rotated with position angle $206.^\circ8$. Some of the resulting mosaics have gaps near the edges of the fields, which depend on the camera. The BRIGHT1 readout pattern was used, with seven groups and one integration per exposure, for 12 total dithers leading to a total exposure time of 1675 s.

Imaging observations with MIRI were first carried out on 2022 August 4–5 using eight filters and are also shown in Table 1. The remnant was covered by a 3×5 mosaic with a four-point dither pattern. The readout pattern was FASTR1, eight groups and one integration per exposure, with four total dithers leading to exposure times of 88.8 s. An additional location was selected well away from the remnant to sample the background.

Unfortunately, there was an error with the tiling pattern of the spacecraft, which introduced gaps in the mosaics and a gradual east-to-west drift between the centers of the FOVs of approximately 16″. We applied and were approved for a return visit to cover the gaps with three additional MIRI pointings per filter. These return observations were conducted on 2022 October 26 and performed with a position angle approximately 90° to the original visit, which made the edges of the detectors parallel. The overlapping field center of all mosaics is approximately α(J2000) = $23^h23^m26.^s97$, δ(J2000) = +58°49′ 08.″6, with the entire FOV spanning approximately $5.'3 \times 5.'7$ and rotated with position angle $131.^\circ5$.

The imaging data were processed using the JWST Science Calibration Pipeline (Bushouse et al. 2022) version 1.8.4 and the calibration reference data system (CRDS) version 11.16.14, with the CRDS context file `jwst_1017.pmap`. Background images were produced from dedicated sky observations and subtracted from the individual images in the `calwebb_image2` pipeline step. We did not subtract background images from the F770W, F1000W, F1130W, and F1280W data due to the variable spatial structure of the sky background at these wavelengths. The level 2 images were astrometrically aligned using the JWST Alignment Tool (Rest et al. 2023).

Mosaic images were then constructed using the default pipeline parameters but with the `tweakreg` and `skymatch` steps turned off. The pixel scales of the final mosaics are 0.″031 pixel^{-1} for the NIRCam SW camera images and 0.″063 for the NIRCam LW camera images. The pixel scale of the MIRI mosaics is 0.″111. Composite images made from the mosaics are shown in Figure 1. Mosaics of individual filters showing the entire FOVs are shown in the Appendix.

Spectroscopy was performed between 2022 August and November with MIRI and the MRS, which is an IFU with a field size that is variable with wavelength ranging from $3.''2 \times 3.''7$ to $6.''6 \times 7.''7$. Three locations were selected after the MIRI imaging observations were available and could be inspected for precise placement with respect to remnant emission: two positions targeted bright ejecta knots in the main shell (P1 and P3), with one targeting newly identified emission toward the projected center of the remnant (P2). An additional observation, P4, was obtained on a location selected using archival Spitzer observations targeting unshocked ejecta in the central region (DeLaney et al. 2010; Isensee et al. 2010). For P1, P2, and P3, a four-point dither was used with the FASTR1 readout pattern, using 50 groups per exposure, for total exposure times of 555 s. Simultaneous imaging was obtained in the F560W, F770W, and F1500W filters. For P4, the total exposure time was doubled, and simultaneous MIRI imaging was obtained in filters F1130W and F1500W.

We used version `1.11.0` of the `jwst` module, which includes the three stages of pipeline processing, and the `jwst_1141.pmap` reference file over the course of the calibration. Stage 1 and stage 2 processing was performed on all four cubes and the designated background with default settings. All cubes ran through `jwst.residual_fringe.ResidualFringStep` and then stage 3 processing. The designated background was used for the master background step for P1, P2, and P3. The master background step was skipped for P4, since the designated background was obtained 3 months after P4 was observed.

The stage 3 pipeline provides the processed data cubes, as well as a 1D extracted spectrum over the entire FOV. We combined all 12 channel and grating settings. A constant was

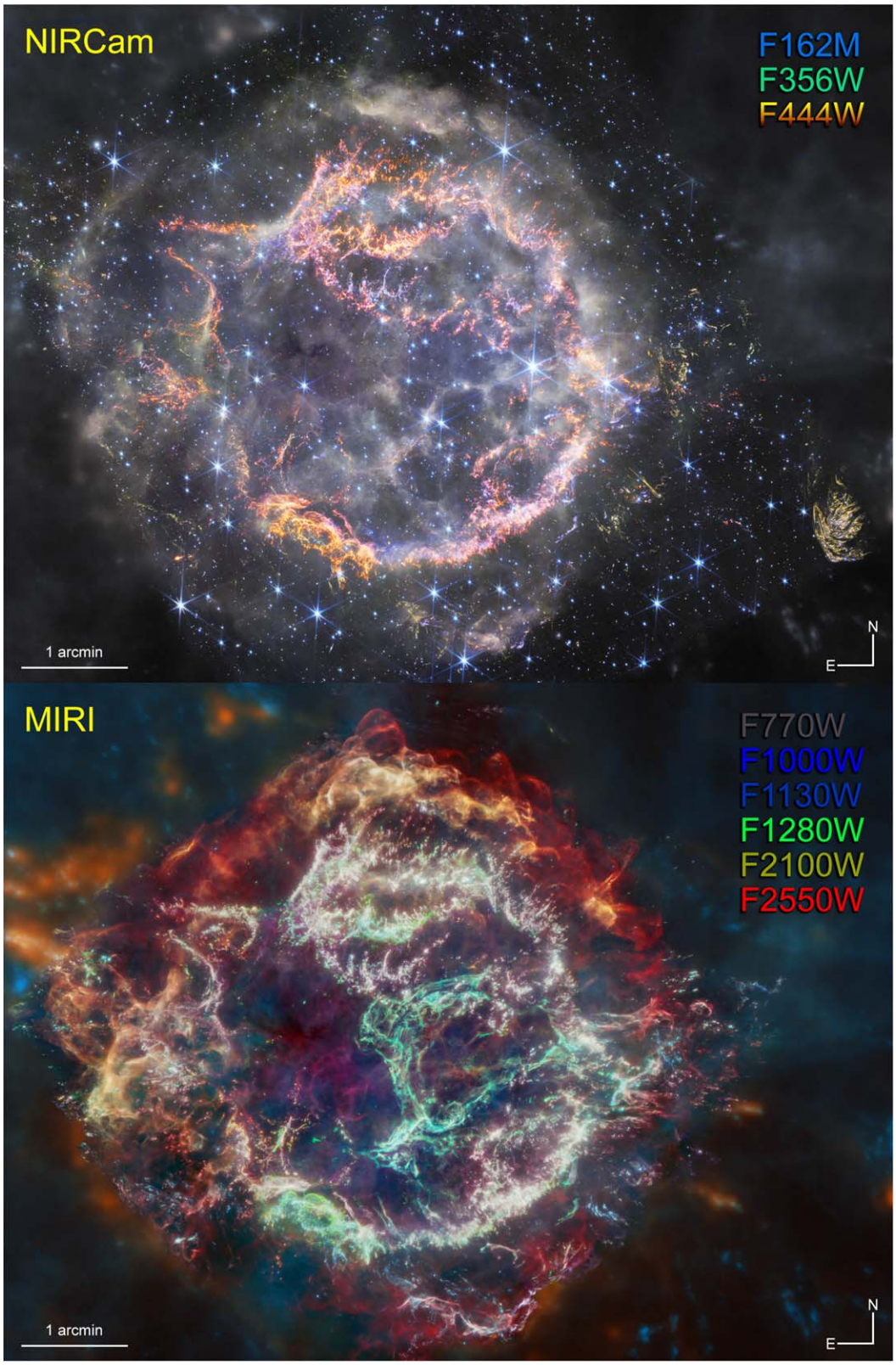

Figure 1. Composite images of our NIRCam (top) and MIRI (bottom) mosaics obtained as part of our JWST survey of Cas A. FOVs have been subtly cropped, and minor corrections have been made to compensate for gaps in coverage. Corners not imaged by JWST have been filled in with archival Spitzer data at comparable wavelengths. Mosaics of all individual filters showing the entire FOVs are shown in the Appendix.

added to each of the four fully combined spectra such that the integrated surface brightness over the F770W transmission curve for each spectrum matches the average surface brightness at the corresponding position measured in the F770W image within a region corresponding to the MRS FOV at this wavelength.

Below, we present and briefly discuss all four MRS spectra, shown in Figure 2, with locations identified in Figure 3. We

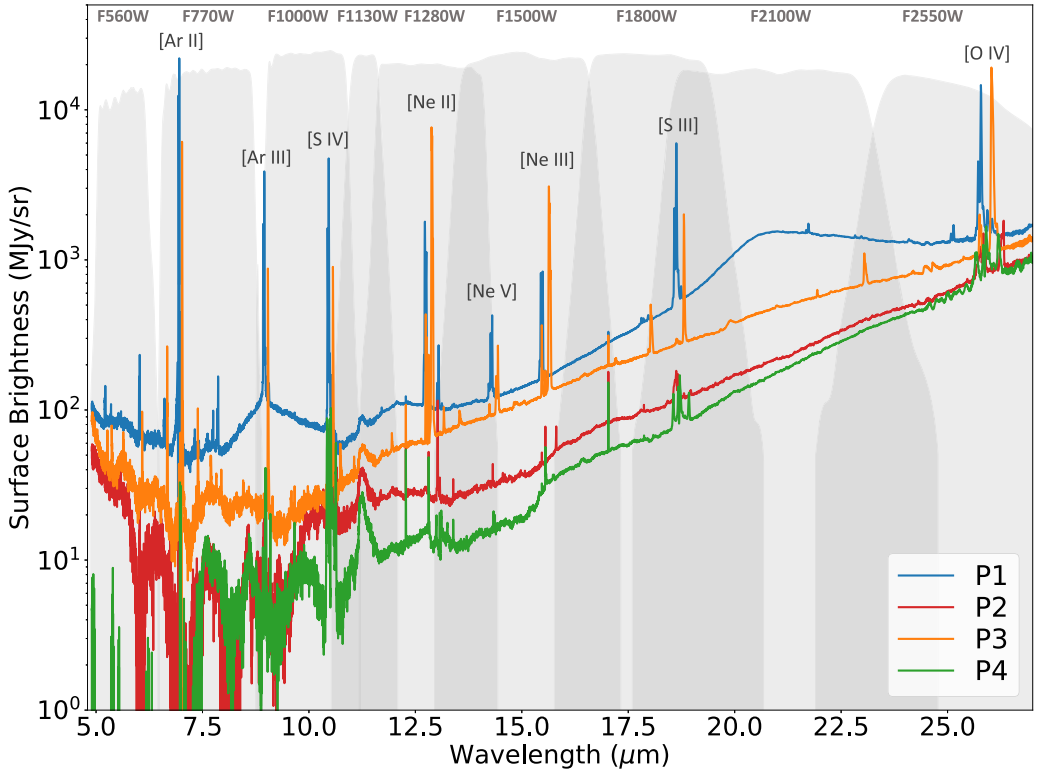

Figure 2. MIRI/MRS spectra obtained as part of the survey. P1 and P3 were selected to sample two shocked ejecta knots of different compositions. P4 represents a "core sample" of unshocked ejecta through the interior of the remnant, and P2 was selected to help diagnose the emission arising in the Green Monster (see Section 3.2). All spaxels of the overlapping FOVs across all four channels have been integrated. Positions with respect to Cas A are shown and labeled in Figure 3. Dominant emission lines from the ejecta are labeled. Bandpasses of the MIRI filters are overlaid with throughputs normalized to arbitrary units. Many of the same emission lines are seen at all four positions, but offsets due to velocity are evident. Dust emission features (listed in Table 1) are seen at all positions with varying intensities and described in more detail in Section 4.1. Note the large dynamic range on the vertical axis.

focus on P2 and P4 within the context of investigating unshocked interior ejecta. I. De Looze et al. (2024, in preparation) provide an in-depth analysis of P2 within the context of interaction between the remnant and the dusty circumstellar environment (see also Section 3), and Rho et al. (2024, submitted) investigate P1 and P3 within the context of molecule formation and destruction.

3. Mosaic Images

Our mosaic images map thermal and nonthermal NIR and mid-infrared emission from Cas A with unsurpassed depth and sensitivity. Table 1 provides a complete log of imaging observations along with sources of relatively strong emission in each filter bandpass. Prominent emission features of these imaging mosaics and discoveries of our survey are highlighted in Figure 3 and discussed below.

3.1. NIRCam

Three filters were selected for the NIRCam mosaics that could distinguish between ejecta, circumstellar material (CSM), dust, and the fundamental vibrational mode of CO centered around 4.65 μm. The F162M filter was selected for its sensitivity to [Si I] 1.645 μm and [Fe II] 1.644 μm emission present in ejecta (Koo et al. 2018), both diffuse and clumped, and He-rich CSM (Koo et al. 2023). The F444W filter is sensitive to multiple emission lines of the ejecta, including magnesium and argon, along with CO emission, synchrotron radiation, and faint dust continuum emission. The F356W filter, which largely serves as a continuum reference for the F444W, is sensitive to relatively weaker ejecta lines, including ones from calcium and silicon, along with dust and synchrotron radiation.

The strongest emission in the NIRCam mosaic (Figure 1) is seen along the main shell of ejecta that has encountered the reverse shock and represents the remnant's densest material ($n \sim 10^{3-5}$ cm^{-3}) with temperatures between 5000 and 10,000 K (Chevalier & Kirshner 1978; Hurford & Fesen 1996; Smith et al. 2009; Lee et al. 2017). As seen in HST data (Fesen et al. 2001), the ejecta are often grouped into large filament complexes of varying scales and are often increasingly dissipated in directions away from the reverse shock (Morse et al. 2004).

The superb resolution of the NIRCam/F162M (0.″055) compared to earlier HST NIR images places a new constraint on the clump size as small as <200 au. Furthermore, NIRCam observations detect numerous ejecta knots beyond the main ejecta shell, many of which have not been previously observed either in HST optical or ground-based NIR observations (Fesen & Milisavljevic 2016; Koo et al. 2018). The knots show different colors in the NIRCam three-color image in Figure 1, suggesting that their elemental compositions are different. The physical and chemical properties of the outlying ejecta knots will be investigated by B.-C. Koo et al. (2024, in preparation).

Outside of the main shell, the remnant is enveloped in synchrotron emission, seen most strongly around the periphery of the main shell (see representative region enlarged in Figure 3, panel (1)) but also interior to the main shell (Figure 1). This is associated with the forward shock interacting with surrounding CSM/ISM. Inside the main shell, diffuse emission

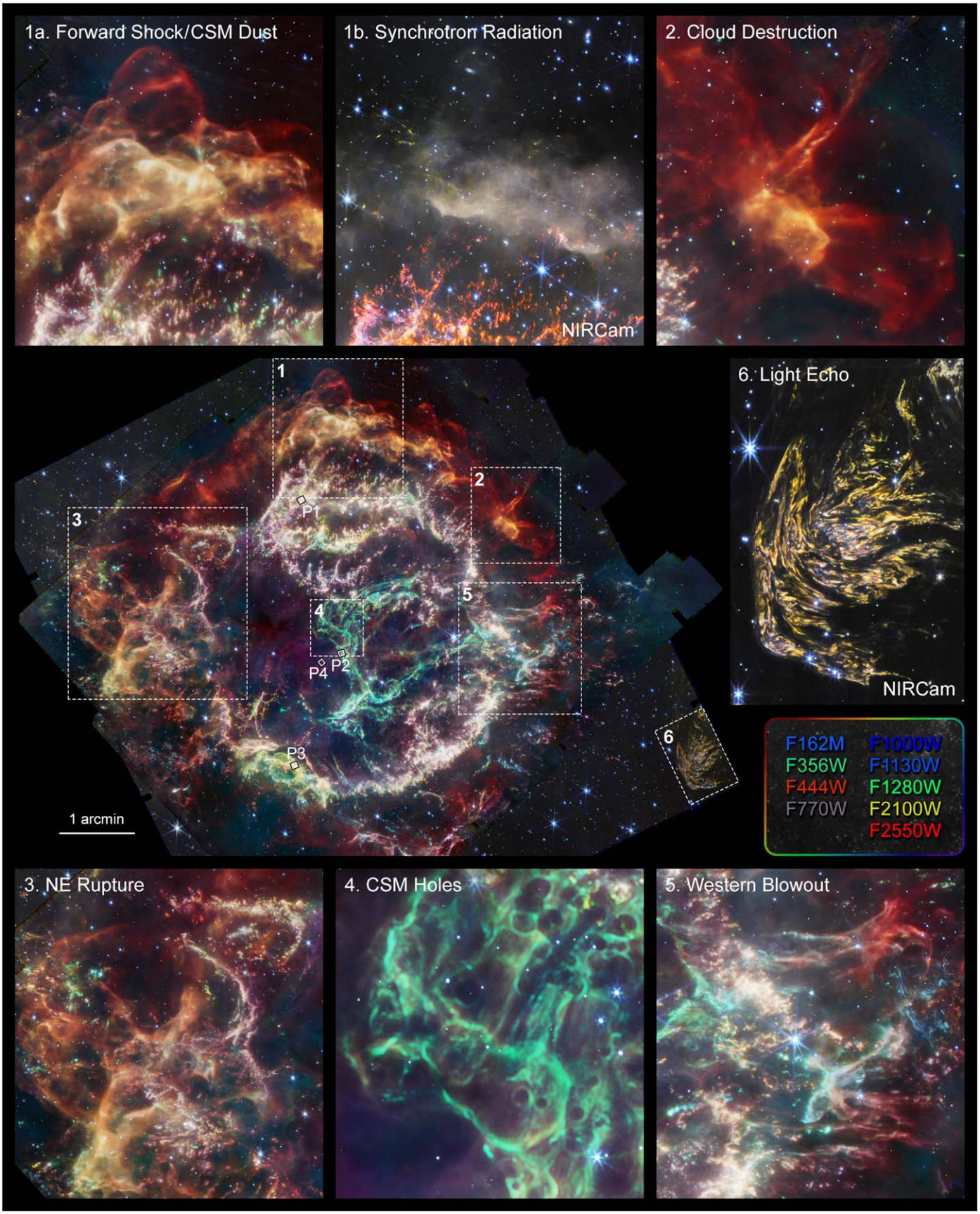

Figure 3. Important features of Cas A identified in our survey and discussed in this paper. The composite image in the center panel combines NIRCam and MIRI filters as indicated. Large boxes outlined with dashed white lines show areas of interest enlarged in the surrounding panels that use the same filters and color scheme, with the exception of panels (1b) and (6), which only use NIRCam filters. Small boxes outlined with solid white lines show the positions of the four regions of MIRI/MRS IFU spectroscopy.

in F162M is a blend of synchrotron and [Fe II]+[Si I] line emission associated with unshocked SN ejecta (Koo et al. 2018). We note that differences in the distribution of interior emission between our F162M image and the long-exposure ground-based image published in Koo et al. (2018) are most likely because they removed *H*-band emission. Additional discussion of the synchrotron radiation is provided in Section 6.

Clumpy N- and He-rich CSM (aka "quasi-stationary flocculi," or QSFs; see van den Bergh 1971; Koo et al. 2018, 2020) appear bright in the F162M image due to their strong [Fe II] lines. This is evident because all prominent QSFs identified in the 2013 ground-based [Fe II] 1.64 μm image by Koo et al. (2018) remain observable in the new JWST data. JWST's resolution exposes intricate morphologies arising from interactions with the SNR shock. Some QSFs have sharp boundaries with abrupt brightness drops implying the presence of unshocked CSM that has not been processed by the shock yet. Scattered throughout the interior are numerous never-before-seen complete and partial rings approximately 1″ in size, associated with emission from shocked CSM, that overlap with holes observed in MIRI images (these features are discussed more extensively below in Section 3.2).

An unexpected result from our NIRCam mosaics was the discovery of abundant light echoes within close proximity to the remnant, including a particularly large and finely structured one ∼4′ southwest of Cas A's center (Figure 3, panel (6)). These light echoes are also observed in our MIRI mosaics in places where the more limited MIRI FOV overlapped with NIRCam. Dozens of light echoes are seen scattered around the periphery and even projected within the main shell, with angular sizes between ∼0.″1 and 1′. Light echoes are discussed in more detail in Section 5.

3.2. MIRI

For MIRI imaging, eight filters were selected to provide a minimal set required to sample and differentiate line emission associated with ejecta and CSM from dust continuum emission. The bright main shell is made up of reverse-shocked ejecta emitting lines associated with oxygen, sulfur, argon, and neon (Ennis et al. 2006; DeLaney et al. 2010) and an overall much stronger contribution from dust (Rho et al. 2008). Clumps of ejecta are seen down to the resolution limit of each image. Dust emission is also present throughout the surrounding CSM that has been heated by the forward shock. Particularly conspicuous is the arc of dust continuum strongest in the F2100W and F2550W filters seen stretching from northwest to east outside of the main shell. Bow shocks bright in dust emission are seen in the north, and in the northwest, a relatively large cloud of CSM has been overtaken and disrupted by the forward shock (Figure 3, panels (1) and (2)).

The strongest emission seen interior to the main shell is concentrated in what we will refer to as the "Green Monster," which extends across the west side of the central region (Figure 3, panel (4)). The emission is seen faintly in earlier Spitzer IRAC and MIPS observations, and the general location overlaps with the characteristic spectra identified by Arendt et al. (2014) as the "South Spot" that was fit with dust compositions similar to the ones found around X-ray Fe ejecta emission. The emission is seen in all filters longward of F1000W, suggesting a dominant dust continuum component. Our JWST observations show, for the first time, the detailed structure of the Green Monster, which is concentrated in long filaments among fainter sheets that together are pockmarked with circular holes ∼1″ in radius. Some of these holes are outlined as rings (partial and complete) in the NIRCam mosaics, especially in the F162M filter.

One possible interpretation of the Green Monster and its unusual pockmarked morphology is that it is associated with unshocked ejecta that have been expanded by small clumps of radioactive material (^{56}Ni or ^{44}Ti). Cas A is already known to have been strongly shaped by large-scale Ni bubbles that expanded into O-, Ar-, and S-rich ejecta, forming large-scale rings as observed in the shocked main shell (Lawrence et al. 1995; Blondin et al. 2001; DeLaney et al. 2010; Milisavljevic & Fesen 2013; Alarie et al. 2014), and cavities as observed in the interior unshocked ejecta (Milisavljevic & Fesen 2015) with radii of 0.′5–1′. Hence, the holes in the Green Monster could be a much smaller-scale version of this phenomenon, induced by extremely finely clumped radioactive material, expanding within the central interior of the remnant.

However, in light of low-velocity ($\lesssim$100 km s^{-1}) emission lines of [Fe II] 1.644, H Brα 4.05, [Ne II] 12.81, and [Ne III] 15.56 μm associated with the small rings (I. De Looze et al. 2024, in preparation), along with the X-ray properties of emission in this region that include correlation with morphology observed in the infrared (Vink et al. 2024; see also Section 6), we instead favor that the dominant emission in the Green Monster region is due to circumstellar gas, rich in dust, that has been excited by the forward shock and sculpted by stellar debris. In this scenario, the central location within the main shell is simply a projection effect, and the holes are the result of small knots ($\lesssim$0.″1) of high-velocity ejecta that have punctured through the CSM and driven expanding tangential shocks (e.g., Orlando et al. 2022).

Finally, an apparent blowout protruding outward from the main shell is seen in the western portion of the remnant (Figure 3, panel (5)). This blowout runs due west and is different from the direction of the known southwest outflow (or "jet"; Fesen 2001; Hwang et al. 2004). The morphology of this western blowout shares some resemblance to the northeast rupture in the main shell (Figure 3, panel (3); see also Fesen & Gunderson 1996), and the general location is known to host a large population of QSFs (Koo et al. 2018). The blowout could be associated with interaction between the remnant and an abrupt density discontinuity in the ISM, not unlike the breakout observed in the northeast section of the Galactic remnant CTB 1 (Fesen et al. 1997). Nonetheless, the MIRI emission in this region has a conspicuous overlap with (i) Si-enriched X-ray-emitting ejecta (Vink 2004) and (ii) the projected trajectories of dozens of high-velocity ($\gtrsim 8 \times 10^3$ km s^{-1}) S-rich ejecta knots moving radially outward from the center of expansion (Fesen & Milisavljevic 2016), which together indicate that the blowout, like the northeast rupture, may reflect structure imprinted by the explosion dynamics of the original SN (Laming et al. 2006).

4. IFU Spectroscopy

Our MIRI/MRS spectra only cover four very small FOVs (channel-dependent, ranging from ∼3.″5 to ∼7″[37]) but have far superior spatial and spectral resolution compared to previous

[37] See the MIRI MRS page in the JWST Documentation for details, https://jwst-docs.stsci.edu/jwst-mid-infrared-instrument/miri-observing-modes/miri-medium-resolution-spectroscopy.

low-resolution 5–38 μm spectral maps of Cas A obtained by Spitzer with the Infrared Spectrograph (IRS; Smith et al. 2009). An overview of the spectra of all four positions is shown in Figure 2. These MIRI/MRS positions sample a diverse range of emission from the remnant and surrounding environment. P1 and P3 were selected as regions covering different elemental compositions of ejecta and dust excited by the reverse shock in the north and south; both the shape of the dust continuum and the relative intensity of the emission lines vary between the two positions. P2 is coincident with one of the small holes of the Green Monster but also samples a column of unshocked ejecta and dust through the center of the remnant. P4 was a "deep drilling" IFU position designed to be primarily sensitive to unshocked ejecta, especially iron, through the center of the remnant. Selection of these areas was guided in part by the Spitzer IRS spectral maps. Based on the in-flight performance report from Argyriou et al. (2023), MIRI/MRS wavelength resolution is accurate to 2–27 km s^{-1}, depending on wavelength, and has a spectrophotometric precision of ≈5.6%.

4.1. Dust Emission

Cas A's young age and proximity make it an ideal target for an in-depth investigation of SN dust formation and destruction processes. Herschel observations were able to probe the cold dust component in the inner unshocked ejecta for the first time (Barlow et al. 2010; De Looze et al. 2017; Priestley et al. 2019) and confirmed the high mass of newly formed dust (0.2–1.0 $M_{\odot}$) but at a limited spatial resolution of ∼0.″6. Similarly, the spatial resolution achieved with Spitzer IRS spectroscopy (2.″5–6″) was insufficient to resolve individual ejecta knots, which made it impossible to constrain the chemical pathways that lead to the formation of specific warm dust species in Cas A. Spitzer IRS did, however, identify the formation of many different dust populations around chemically distinct regions in Cas A (Rho et al. 2009; Arendt et al. 2014). JWST can associate spatially resolved warm dust knots with different chemical compositions (Ar, Ne, S, O) and has the sensitivity to detect distinct dust emission features in those individual knots. The detailed analysis of the MRS dust emission and decomposition of the various dust species that condensed in the ejecta of Cas A will be presented in a future publication. Here, we summarize the general properties of the dust emission observed with MRS and compare them to previous studies with Spitzer.

The MIRI/MRS spectra in Figure 2 all show a continuum from warm dust grains and various dust emission features. Position P1, which samples reverse-shocked ejecta with particularly bright argon emission, shows prominent broad dust features at 9, 12, and 21 μm. Arendt et al. (2014) attributed the 9 and 21 μm features to $Mg_{0.7}SiO_{2.7}$ grains characterized by a relatively low magnesium-to-silicon ratio, while Rho et al. (2018) attributed the features to SiO_2 grains. Arendt et al. (2014) argued that the 12 μm feature could arise from ellipsoidal SiO_2 or SiC grains with a continuous distribution of axial ratios, and that the dust with this spectral profile is likely a mixture of silica and Mg silicates with Mg/Si < 5. The MRS spectra show that this 12 μm feature is likely present in all four positions in Cas A, while the 9 and 21 μm features are only apparent in the argon-rich ejecta. The narrow dust feature at 11.3 μm that is likely produced by SiC grains (e.g., Jiang et al. 2005) is also present in all four spectra shown in Figure 2. We note that the same complex of dust emission features (9, 11.3, 12, and 21 μm) is present in the spectrum of newly condensed SN dust in SNR G54.1+0.3 (Temim et al. 2010), which may be evidence that these features all arise from a common grain species or that the multiple grain species that produce the set of features are often found in the same environment.

Position P3 also samples reverse-shocked ejecta, but it is centered on a region that is neon-bright. This region is characterized by a smooth and featureless dust continuum that is clearly very different from position P1. The continuum emission at positions P2 and P4 that sample the remnant interior and the Green Monster region both show similar shapes with a "knee" in the spectrum around ∼16 μm. Interestingly, the shape of the dust spectrum in these interior positions is most similar to the Spitzer-observed spectrum arising from Cas A's CSM component, which Arendt et al. (2014) fitted with either $MgFeSiO_4$ or $Mg_{2.4}SiO_{4.4}$ as the dominant dust constituent.

In addition to providing a unique view of dust composition variations, the extensive imaging of Cas A with JWST allows the small-scale structures of the freshly condensed ejecta dust to be resolved at unprecedented spatial scales. The high resolution of MIRI images allows ejecta knots to be resolved down to sizes of (1–4) × 10^{16} cm (or 0.003–0.013 pc), with NIRCam pushing this resolution limit to 6 × 10^{15} cm (or 0.002 pc) at 3.56 μm. Where HST was able to resolve line-emitting ejecta knots down to similar scales, JWST provides a complementary view of the dust-emitting structures in the ejecta. Comparison of the specific dust compositions with the distribution and elemental abundances of certain elements on resolved scales can provide us with clues on how dust condensation proceeds. Future work can also use these JWST observations of Cas A to address the predominant question of how much freshly condensed dust will survive passage of the reverse shock. Model estimates for Cas A predict a wide range of survival rates (1%–50%; Biscaro & Cherchneff 2016; Bocchio et al. 2016; Kirchschlager et al. 2019; Slavin et al. 2020). These estimates depend sensitively on their assumed preshock grain size distribution and the clump sizes, along with the density contrast between ambient ejecta and dense knots (Kirchschlager et al. 2023). JWST can resolve the shocked dust emission in ejecta knots down to scales that constrain these parameters with measurements that to date have been impossible to obtain.

4.2. Interior Unshocked Ejecta

State-of-the-art core-collapse simulations are having increased success reproducing full-fledged explosions in 3D and are beginning to evolve explosions from core collapse to the SNR phase to allow direct comparisons with observations (Hungerford et al. 2003, 2005; Ellinger et al. 2012, 2013; Wongwathanarat et al. 2013; Janka et al. 2016; Powell & Müller 2019; Burrows et al. 2020; Ono et al. 2020; Orlando et al. 2020, 2021; Vance et al. 2020). The specific explosion mechanism(s) and appropriate treatment of physics enabling the forward shock to overcome the ram pressure of infalling outer layers remain uncertain. A neutrino-driven explosion aided by asymmetries is generally favored for Cas A (Hungerford et al. 2005; Young et al. 2006; Wongwathanarat et al. 2017; Vance et al. 2020), but other explosion mechanisms could participate or even dominate. For example, the two Si-rich wide-angle jetlike outflows of Cas A in the northeast and

southwest (Fesen 2001; Hwang et al. 2004) may be the result of magnetohydrodynamic jets (Khokhlov et al. 1999; Maeda & Nomoto 2003; Couch et al. 2009; Soker 2018) or reflect disk accretion of fallback matter by the newborn NS (see Section 7). A thermonuclear explosion (Kushnir & Katz 2015) or quark nova (Ouyed et al. 2011) have also been suggested.

The relative yields and distributions of elements, including radioactive nuclei freshly synthesized during the SN such as ^{56}Ni and ^{44}Ti (and their decay products) that originate from the innermost regions of the star where the explosion initiated, provide valuable constraints for these simulations (Grefenstette et al. 2014, 2017; Wongwathanarat et al. 2017; Fryer et al. 2023; Sieverding et al. 2023). Hundreds of years after the SN, these nuclei continue to reflect the physical processes dominating the physics of SN engines and probe the degree of explosion asymmetry. Particularly important is the mass and distribution of Fe. The X-ray-bright reverse-shocked Fe-rich ejecta of Cas A (which traces the original ^{56}Ni distribution) has velocities around and above 4000 km s^{-1} (Hughes et al. 2000; DeLaney et al. 2010) and is associated with a mass of $\approx$0.13 $M_{\odot}$ (Hwang & Laming 2012), which is a fair fraction of the total amount of Fe expected to have been ejected in a neutrino-driven explosion of about 2×10^{51} erg as estimated for Cas A (Orlando et al. 2016). For this reason, Cas A has been used as a clear example of how the ejecta asymmetries connected to the neutrino-driven mechanism and the nature of the progenitor as a H-stripped star can strongly influence the final distribution of ejecta by seeding Rayleigh–Taylor instabilities that in turn encourage radial mixing (Wongwathanarat et al. 2015, 2017).

Presently, uncertainties in theoretical models (due to both the unknown exact mass and structure of the progenitor and uncertain degrees of freedom in the neutrino physics of SN calculations) leave it unclear how much unshocked Fe is expected, and observations have been unable to derive how much is actually present in Cas A (e.g., Young et al. 2006; Eriksen et al. 2009). Multiple lines of evidence support the notion that some Fe must still reside in the center of Cas A (see, e.g., Hwang & Laming 2012; Milisavljevic & Fesen 2015; Grefenstette et al. 2017). However, how much and how it is distributed are critical unknowns. By measuring the iron abundance, we obtain a better understanding of the nature of the central engine. Among the best efforts to date to investigate unshocked Fe was a deep 1.64 μm image of Cas A by Koo et al. (2018), which likely traced interior [Si I] 1.645 μm line emission as opposed to the [Fe II] 1.644 μm line, and Laming & Temim (2020), who used Spitzer IRS spectra of Cas A. Laming & Temim (2020) estimated the total unshocked ejecta mass to be $0.47^{+0.47}_{-0.24}$ $M_{\odot}$, which was broadly consistent with previous estimates (Hwang & Laming 2012; DeLaney et al. 2014; Arias et al. 2018) and with mass fractions of 30% O, 60% Si, a few percent S, and traces of Ne and Ar. No Fe was confidently detected in the Spitzer data, but possible features at [Fe VIII] 5.446 and [Fe V] 20.85 μm along with other considerations led to an upper limit Fe mass of $<$0.07 $M_{\odot}$ (Laming & Temim 2020).

We examined MIRI/MRS spectra of P2 and P4 closely for possible emission features around the [Fe VIII] 5.446 and [Fe V] 20.85 μm emission lines. The only possible candidate is faint emission peaked around 5.39 μm observed only in the P4 region potentially associated with blueshifted [Fe VIII] 5.446 μm. A second, weaker emission peak is also observed at 5.53 μm. The distribution of emission around these candidate lines is unlike other ejecta lines that are narrower and better resemble what would be expected from PAHs, though none are documented at these wavelengths. Nonetheless, if this emission originates from truly diffuse, extended gas, then the observed distribution is viable. Following assumptions in Laming & Temim (2020) that emission lines come from density regions where their emission is maximized, we estimate that the putative [Fe VIII] emission in the P4 FOV (approximately 7×10^{-7} erg cm^{-2} s^{-1} sr^{-1}) represents $\sim 10^{-5}$ $M_{\odot}$ of Fe. If replicated similarly across the remnant, this would imply $\sim 10^{-2}$ $M_{\odot}$ of unshocked Fe material. However, since the candidate emission feature is absent from the P2 spectra, the Fe is clearly not distributed uniformly. Future work can investigate the reality of this candidate detection and carefully utilize all available images and spectra to develop the best constraint possible of the total Fe yield from the SN.

Another potential marker of unshocked ejecta available in the JWST range is the relatively bright [O IV] 25.89 μm line emission (Figure 2). Even though ejecta interior to the main shell are unshocked, they are still ionized by the UV and X-ray emission from the surrounding reverse shock, resulting in [O IV]. The F2550W filter is sensitive to [O IV], with an additional contribution from dust continuum emission. As seen in Figure 2, the F2100W filter primarily samples dust continuum emission. By using the F2100W image as a continuum reference and scaling appropriately to match the general continuum level of F2550W, the result of F2550W − F2100W should primarily arise from [O IV].

We present this map of unshocked ejecta in Figure 4. A remarkable, asymmetrical, weblike network of filaments resolved to 0.01 pc scales is seen interior to Cas A's main shell of reverse-shocked material. Many ejecta streams directed outward from the center of expansion are seen, including a thin filament that runs directly toward the center of the northeast rupture ("NE filament"), a branch of emission that runs almost due west ("western branch"), and multiple filaments extending in the southeast direction toward the high-energy ejecta plumes of iron observed in the X-ray ("SE filaments") (Hughes et al. 2000; DeLaney et al. 2010; Sato et al. 2021). A variety of rings/loops with scales of $\approx$5″ are embedded within these filaments. An especially bright arc of looped filaments is seen east of the main shell center (labeled "central arc"). We interpret the significance of this structure in the context of additional multiwavelength comparisons in Section 6.

We note that portions of our unshocked ejecta map may be contaminated by cold dust embedded in the interior ejecta, as well as emission from filaments of shocked ejecta. However, many arguments strongly support the view that the dominant emission is indeed from unshocked ejecta. For example, the bright "central arc" is consistent with interior structure already mapped in [S III] $\lambda\lambda$9069, 9531 by Milisavljevic & Fesen (2015) having a velocity distribution of $-$3000 to $+$4000 km s^{-1}. Likewise, the distribution of emission in our unshocked ejecta map strongly correlates with features interior to the main shell only seen in the [S IV]-sensitive F1000W image.

The centrally located P2 and P4 MIRI/MRS spectra provide a complementary probe of the unshocked ejecta through the center of the remnant. We isolated [O IV] emission in each spaxel by exploring the data cube with the STScI-developed JDAViz tool (JDADF Developers et al. 2023) to find appropriate wavelength regions to model the continuum. A third-order polynomial was used for the continuum fit, which was then subtracted from the data cube. The cube was cropped by $\sim$3 pixels on each side to

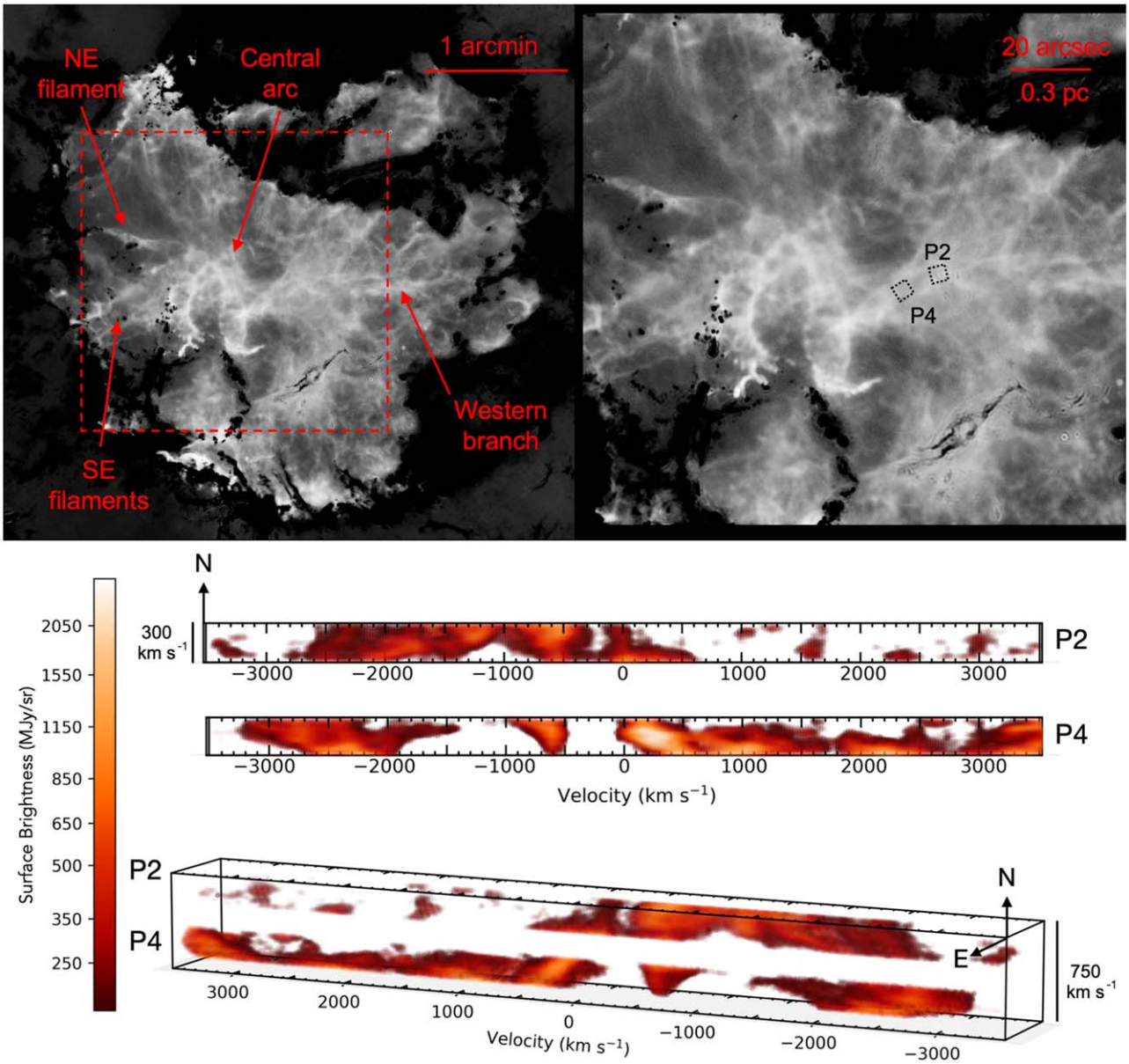

Figure 4. Mapping unshocked ejecta of Cas A. Top: image resulting after subtraction of a scaled version of the F2100W filter from F2550W and masking main shell emission (which appears as black). The emission inside the main shell is mostly due to [O IV] 25.89 μm from unshocked oxygen material, with potential minor contributions from cold dust, line emission from filaments of shocked oxygen ejecta, and line emission from other shocked/unshocked material including iron. The dashed box indicates the region enlarged in the right panel, and the labeled boxes identify MIRI/MRS IFU regions. Bottom: a 3D reconstruction of the MIRI/MRS [O IV] 25.89 μm emission from P2 and P4 as a function of velocity showing the wide spread of the ejecta in velocity space. Emission $>3\sigma$ above the continuum level is represented.

eliminate artifacts from the edge of the detector. Coordinates in R.A. and decl. were converted into velocity using the scaling factor of 0.″022 per km s^{-1} (Milisavljevic & Fesen 2013) with respect to the center of expansion (Thorstensen et al. 2001). The data were linearly interpolated and resampled with a resolution of 22 km s^{-1} in all three dimensions, which is comparable to the original spatial resolution.

The continuum-subtracted, cropped, interpolated [O IV] emission from P2 and P4 as a function of velocity is shown in the bottom of Figure 4 from two viewing angles. Previous observations by Spitzer using the IRS presented by Isensee et al. (2010) with a spatial resolution of 2.″5 and spectral resolution of 0.05 μm indicated sheetlike structures and filaments, including holes within the sheets at the scale of 30″. Our data, which localize ejecta velocities with an uncertainty of $\lesssim$160 km s^{-1} for any 3D location of the [O IV] emission and improve over Spitzer observations by approximately an order of magnitude, reveal an even more intricate distribution with filaments seen at the scale of 1″. The velocities range over $\pm$3000 km s^{-1}, indicative of ejecta and not CSM. We interpret the MIRI/MRS spectra as further confirmation that the interior network of filaments seen in the top panel in Figure 4 traces unshocked ejecta accurately.

The [O IV] emission is accompanied by fainter emission in the [S IV] 10.521, [S III] 18.676, and [Ar III] 21.823 μm lines. Their spatial structure within the IFU field and their velocity

structure are nearly identical to those of [O IV], implying that these elements are thoroughly mixed down to the scale of the JWST resolution. In photoionization equilibrium in Cas A, these ions exist at densities in the range of 1–20 amu cc^{-1} and temperatures from about 20,000 K down to 600 K (Laming & Temim 2020). This gas fills around 20% of the volume. If higher-density gas were present, the [Ar II] 6.9842 μm line would be visible, but only a very narrow line from the background or photoionized CSM is seen. There is no emission from Ne or the [Fe II] and [Fe III] lines in the spectra of the unshocked ejecta, whereas they are seen in the shocked ejecta at P1 and P3. Together, this indicates that substantial abundance variations occur on larger scales.

5. Light Echoes

Transient luminous sources such as novae and SNe can produce echoes of their outbursts by way of reflected light from dusty regions in the surrounding ISM (van den Bergh 1965; Rest et al. 2005; Dwek & Arendt 2008). Light echoes have been recorded around Cas A, and spectra of them have been used to classify the explosion type (Krause et al. 2008), measure explosion asymmetry by observing the original SN from different lines of sight (Rest et al. 2011), and probe the structure of the surrounding ISM itself (Kim et al. 2008; Besel & Krause 2012; Vogt et al. 2012). Generally, emission at $\gtrsim$3 μm is likely to be reradiated thermal emission from dust, whereas the shorter-wavelength emission is more likely to be scattered light of the transient source itself. Light echoes can be recognized by their structure (more sharply defined than ISM features), spectral energy distribution (warmer than typical ISM), and most clearly by their dramatic brightness changes (when data are available at multiple epochs).

Echoes of various brightness are found across the field of our JWST observations. Figure 5 highlights two prominent regions of echoes. The region labeled E2 shows typical bright echoes, which appear as bright clumps embedded in fainter, more filamentary structures. The additional JWST observations discussed in Section 2 were performed 109 days following the initial observations, providing an unexpected opportunity to search for variations of light-echo features surrounding portions of Cas A. The lower right panel in Figure 5 shows the dramatic changes seen in the MIRI F770W images between these two epochs. These can be confidently identified as light echoes since the proper motion of emission, if interpreted as the same clumps of material from one epoch to the next, would imply unrealistic velocities between 0.3c and 0.6c. The fastest-moving ejecta in Cas A is traveling at 0.05c in the outermost portion of the northeast jet (Fesen & Milisavljevic 2016).

Even more surprising was the appearance of a particularly large and bright IR echo in the corner of the NIRCam field (Figure 3, panel (6)), enlarged in Figure 5. Comparison with archival Spitzer observations confirms that this emission was not present previously, and detection across multiple filters ensures this is a real feature. Recent HST imaging in 2022 December (GO 17210; PI: Fesen) also weakly detected this new light echo, further verifying its reality. An echo this close to Cas A ($\approx$4′ from the center of expansion) means the reflecting surface is almost directly behind the remnant ($\sim$170 lt-yr; see further Dwek & Arendt 2008). In this orientation, the echoing ellipsoid provides a tomographic slice of that portion of the ISM, nearly in the plane of the sky.

The incredible structure in this echo, showing many small isolated features and concentric arclets, along with its overall well-defined outer edge, indicates a very complex ISM cloud surface. The thinnest strands remain unresolved in width even in our NIRCam F162M image. To our knowledge, this is the best view yet of ISM structure at the smallest of scales possible: 0.″1 translates to $\approx$350 au, or $\sim$2 lt-day, which is consistent with the echoes changing completely on timescales of months (Dwek & Arendt 2008), and implies that changes on timescales of hours are possible. The F162M was observed in parallel with both the F356W and F444W observations, which occurred 19.3 hr apart in the initial mapping. Comparison of the F162M images of the large IR echo at these epochs does not reveal any very short-term changes in the echo brightness. This suggests that there were no major changes in the illuminating SN emission on this timescale and/or that the echoing structures are $\gtrsim$19 lt-hr $\simeq$140 au in size. However, F162M is not the band that is most sensitive to the echo emission.

It is worthwhile to note that Krause et al. (2005) had speculated that some of the echoes may have been produced more recently ($\sim$1952) by an unseen or highly directional burst from the NS. Although Dwek & Arendt (2008) and Kim et al. (2008) discounted this possibility based on the geometry and energetics required to fit the IR spectra, some suspicion lingers due to the locations, morphology, and apparent motion of some echoes, which give the visual impression that they lie within the circumstellar environment and thus must be of recent origin. Optical (i.e., reflected) spectra of these echoes in the immediate vicinity of Cas A would definitively determine if they are the product of the Type IIb SN explosion (Krause et al. 2008) or a more recent NS outburst of some kind.

6. Multiwavelength Comparisons

Cas A exhibits complex and overlapping sources of thermal and nonthermal radiation arising from ejecta, CSM, dust, molecules, and particle acceleration. Comparing our JWST infrared observations with Chandra X-ray Observatory and Jansky Very Large Array (VLA) radio telescope data make it possible to disentangle these many sources of emission.

Cas A is one of the brightest radio sources on the sky (Reber 1944), having a total flux density of $\sim$2000 Jy in the 1–2 GHz band (Baars et al. 1977). A relatively circular region with a radius of $\sim$100″ is associated with the reverse shock propagating into the expanding ejecta. Weaker radio emission associated with synchrotron radiation (Ginzburg & Syrovatskii 1965) is seen at some azimuths extending out $\sim$150″ to the location of the main forward shock, traveling at 4200–5200 km s^{-1} (DeLaney & Rudnick 2003; Patnaude & Fesen 2009).

Infrared emission shortward of about 5 μm is known to be largely synchrotron emission from electrons accelerated in shocked regions (Jones et al. 2003; Rho et al. 2003). Earlier Spitzer observations with IRAC at 3.6 μm were observed to resemble radio synchrotron images (Ennis et al. 2006). A more recent study involving radio and Spitzer IRAC data revealed evidence for spectral flattening from a spectral index of $\alpha \approx 0.77$ in the radio to $\alpha \approx 0.55$ for the radio-to-infrared comparison, in particular for those regions close to shock regions (Domček et al. 2021). However, in the southeast region, the synchrotron spectra are relatively steep, $\alpha \approx 0.67$, perhaps indicating the onset of synchrotron cooling. Synchrotron cooling should affect the synchrotron spectrum for frequencies $\nu \gtrsim 7.2 \times 10^{13}\, B_{\rm mG}^{-3} t_{100}^{-2}$ Hz, with $B_{\rm mG}$ being the magnetic field strength in

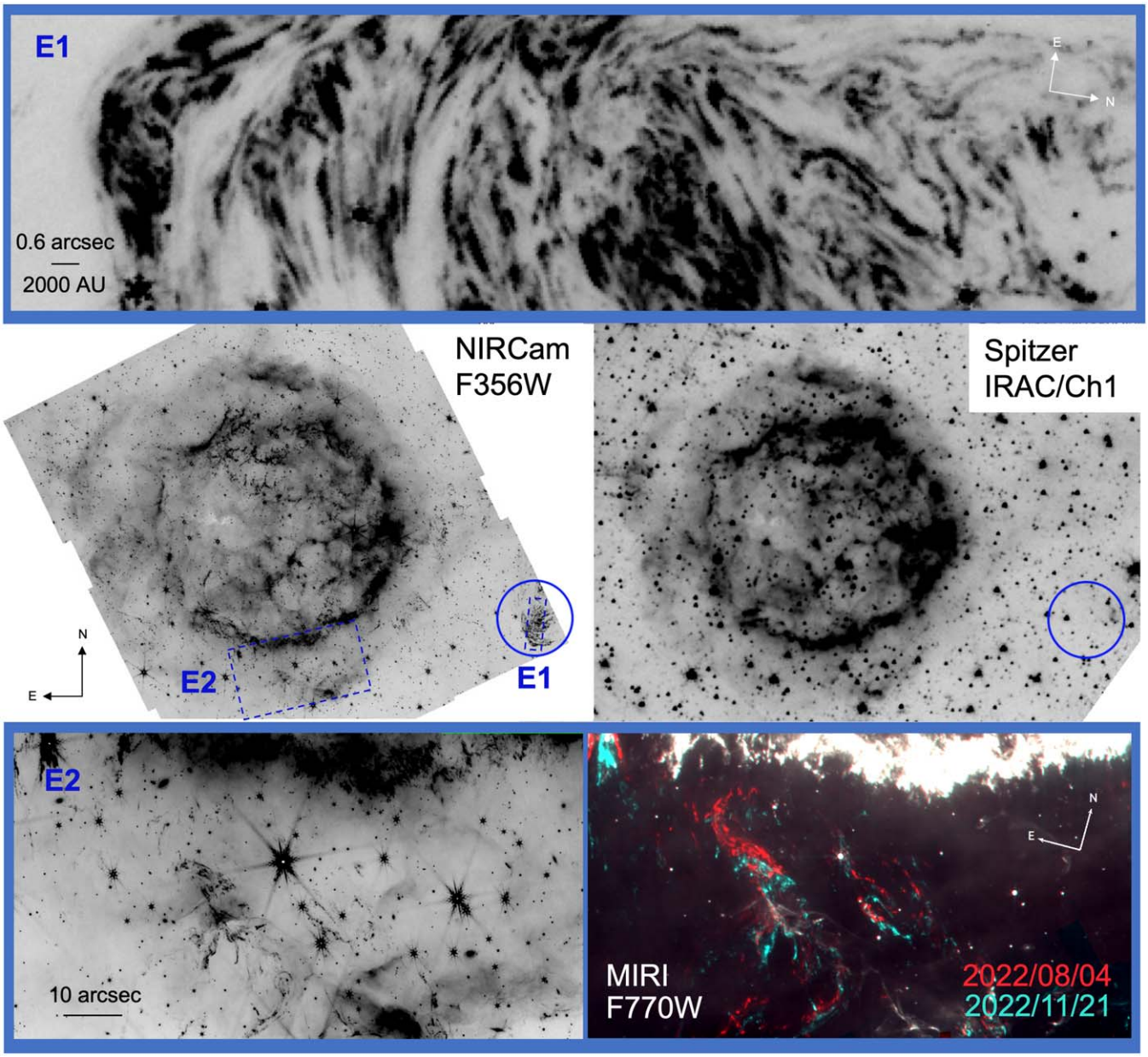

Figure 5. Examples of light echoes around Cas A. The top panel shows an enlarged section of the largest IR echo identified in the middle panels as E1. Comparison of our NIRCam F356W image with archival Spitzer IRAC observations (center) shows that the emission was not present in the past. The boxed region E2 highlights an area where multiple epochs of MIRI observations are available and the time variability of the light echoes can be tracked; this region is enlarged in the bottom two panels. In the bottom right panel, sources with negligible proper motion between the 109 days separating the MIRI F770W observations appear white, whereas light echoes appear as red and teal between the first and second observation. The astrometric shift observed in the emission between the two epochs is associated with apparent velocities between 0.3c and 0.6c, which are too large to be motion of SN ejecta.

milligauss (mG) and t_{100} being the age of the shocked plasma in units of 100 yr. The F356W filter corresponds to $\nu \approx 8.4 \times 10^{13}$ Hz. This implies that signatures of synchrotron cooling can be present for the plasma containing relativistic electrons that have been accelerated early on ($t_{100} \approx 3$) and/or for $B \gtrsim 1$ mG. For comparison, estimates for the mean magnetic field strength in Cas A are ~0.5–1 mG (e.g., Rosenberg 1970; Vink & Laming 2003; Uchiyama & Aharonian 2008).

In Figure 6 (upper panels), we show the NIRCam F356W image alongside an S-band VLA image of Cas A. The increase in sensitivity and spatial resolution of JWST over Spitzer is clear in JWST's ability to map the faint, extended synchrotron radiation component. At least at a qualitative level, these images also reveal patches of low infrared synchrotron surface brightness in the southeastern region, in agreement with Domček et al. (2021). However, a more quantitative analysis accounting for the variable background level is required to provide solid evidence for synchrotron cooling effects in the southeastern region, and perhaps elsewhere.

Other striking morphological features, most likely associated with synchrotron radiation, are the conspicuous cell-like patterns concentrated in the central southwest region (Figure 6). Although these features appear to have a radio counterpart, the contrast between the patterns and more diffuse synchrotron emission is lower. A preliminary explanation for the infrared pattern is that it is the consequence of regions observed edge-

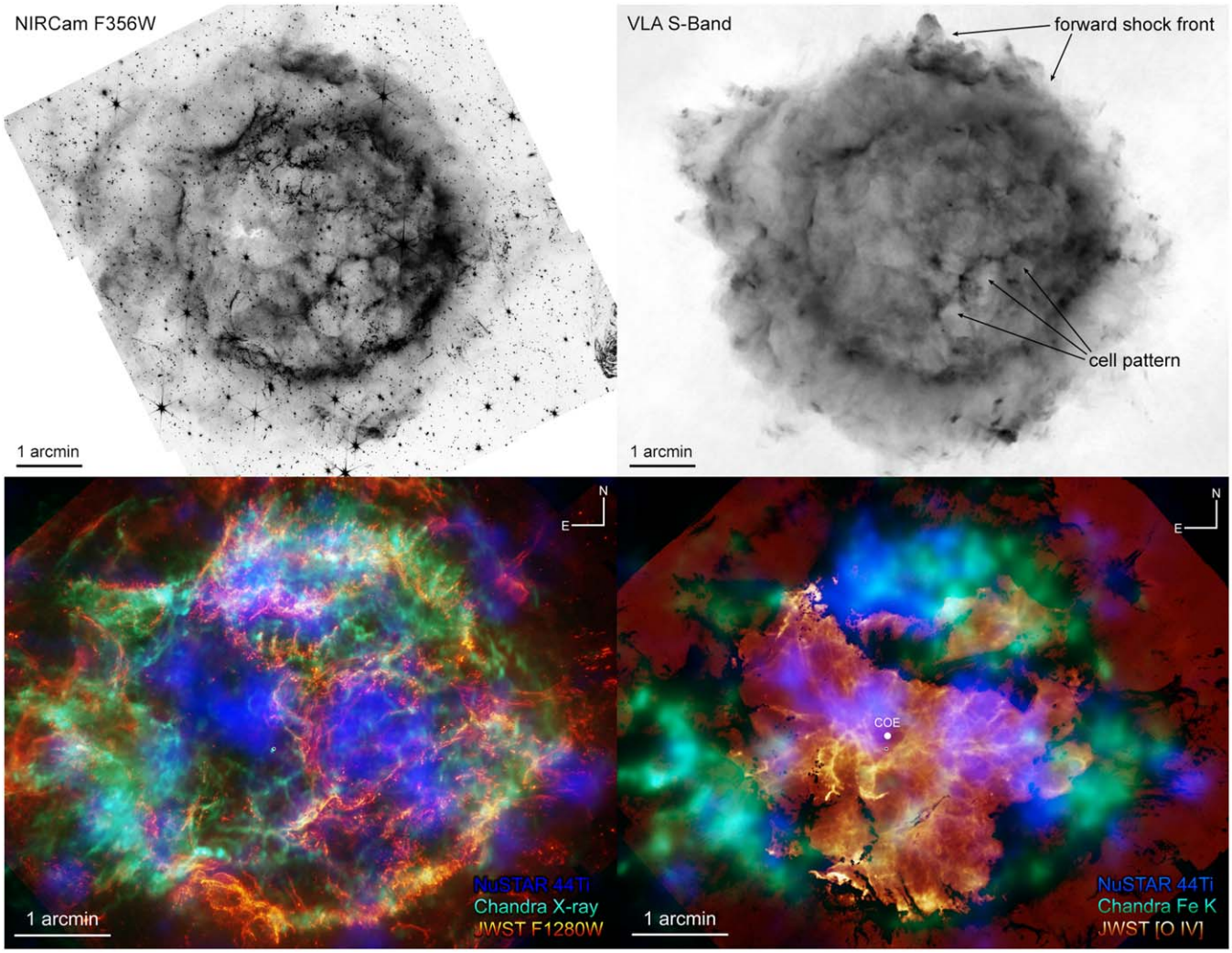

Figure 6. Top: the NIRCam F356W image compared to a VLA *S*-band image from 2012 (courtesy of T. DeLaney). Bottom: the left panel shows a composite image made using the NuSTAR ^{44}Ti map (Grefenstette et al. 2014), the Chandra 1 Ms X-ray image of Cas A (Hwang et al. 2004), and our MIRI F1280W image. The location of the NS (Fesen et al. 2006b) is marked with a black circle. The right panel shows a composite image combining our unshocked ejecta map (see Section 4.2) with the NuSTAR ^{44}Ti map and a Chandra Fe-K map (energy ∼6.7 keV). The locations of the center of expansion (COE; Thorstensen et al. 2001) and the NS are marked with white and black circles, respectively.

on, perhaps associated with blowout regions on the near or far sides of Cas A or with protrusions in the reverse shock (Blondin & Ellison 2001; Mandal et al. 2023). If the infrared synchrotron emission from these regions is affected by synchrotron cooling, then the shells surrounding these blowout regions are narrower in the infrared than in the radio, providing stronger limb-brightening effects. Portions of the cell pattern align with X-ray synchrotron filaments, for which synchrotron cooling effects are even more prominent.

In Figure 6 (lower left panel), we show a composite image using 0.3–10 keV Chandra broadband observations (Hwang & Laming 2012), a NuSTAR ^{44}Ti map (Grefenstette et al. 2014), and our MIRI F1280W image. A gap in the ^{44}Ti emission that runs north–south is approximately where the brightest ridge of the Green Monster is located. Because we favor the interpretation that the bulk emission of the Green Monster is associated with CSM on the front side of the remnant (toward us), the anticorrelation with ^{44}Ti (which is redshifted overall; Grefenstette et al. 2017) should be coincidental. Absorption of ^{44}Ti emission (≈70 keV) from the Green Monster seems unlikely, since a CSM column density of $\sim 10^{27}$ cm^{-2} would be needed to reduce the flux by a factor of 10. Nonetheless, clear correlations in emission are seen between Chandra and our JWST data, suggesting a shared origin. De Looze et al. (2024, in preparation) and Vink et al. (2024) investigate this X-ray–IR relationship in detail and attribute it to interaction between the forward shock and relatively dense CSM.

Another composite image is shown in Figure 6 (lower right) that compares our unshocked ejecta map (Section 4.2; Figure 4) with a Chandra Fe-K map (energy ∼6.7 keV; tracing where ^{56}Ni was produced) and the NuSTAR ^{44}Ti map. As noted earlier, the southeast filaments and western branch of the unshocked ejecta connect with Fe-rich locations. On the other hand, no strong relationship is seen between [O IV] and ^{44}Ti, except that ^{44}Ti emission is located where [O IV] is weak. Together, these comparisons support the view that the fine structures in the interior volume are most likely rooted in turbulent mixing of cool, low-entropy matter from the progenitor's oxygen layer with hot, neutrino and radioactively heated high-entropy matter.

7. NS

First-light images of Cas A taken by Chandra revealed a central X-ray point source (Tananbaum 1999; Pavlov et al. 2000) that is presumably its remnant NS. This NS is part of the family of enigmatic *central compact objects* (CCOs), which are young, exhibit X-ray emission that is steady and predominantly thermal, and lack surrounding pulsar wind nebulae and counterparts at other wavelengths (Pavlov et al. 2004; Halpern & Gotthelf 2010; De Luca 2017). CCOs have relatively low inferred magnetic fields, $B \sim (3\text{–}10) \times 10^{10}$ G, for the three CCOs where it was estimated (i.e., 2 orders of magnitude lower than that of a typical young NS) and X-ray luminosities larger than their spin-down power (Gotthelf et al. 2013).

Deep HST NICMOS images of the Cas A center in NIR filters (Fesen et al. 2006b) did not detect the CCO. The JWST NIRCam images enable a much deeper look at the CCO of Cas A, which is regarded as a key object to understanding NS evolution. The Cas A CCO is the youngest of the dozen currently known CCOs, as well as the youngest of all the known NSs for which we can directly study the surface emission. It is particularly interesting because it has possibly shown a noticeable cooling during the 20+ yr of Chandra observations (Shternin et al. 2023, and references therein; but see Posselt & Pavlov 2022 and Alford & Halpern 2023).

Because ongoing accretion can be excluded for CCOs (Pavlov et al. 2004), their thermal X-rays are likely emitted from the NS surface layers heated by the heat transfer from the cooling NS interiors. The low magnetic fields of CCOs can be explained by two scenarios: (1) these NSs are born with weak magnetic fields ("antimagnetars") or (2) the normal ($\sim 10^{12}$ G) or strong ($\gtrsim 10^{14}$ G) magnetic field of a newborn NS has been buried in its crust by "fallback" debris after the SN explosion (Viganò & Pons 2012). Such fallback could also form a disk surrounding the NS. Comprehensive searches at X-ray and radio wavelengths have failed to find evolutionary descendants of these young CCOs (Gotthelf et al. 2013). Disk emission in the IR would strongly support the reemergence of the magnetic field scenario and explain why it is so difficult to identify CCO descendants.

Nondetections outside the X-ray range are usually attributed to a lack of pulsar activity because of the low magnetic field or high extinction (Pavlov et al. 2004; Halpern & Gotthelf 2010; De Luca 2017). Our NIRCam images offer the possibility to peer deeply enough through high extinction at wavelengths other than X-rays to test hypotheses about the CCO's nature. To this end, we conducted forced photometry at the coordinates of the CCO (α(J2000) = $23^{\rm h}23^{\rm m}27\overset{\rm s}{.}943$, δ(J2000) = $+58°48'42\overset{''}{.}5$; Fesen et al. 2006b) on the three NIRCam filter images using the *space_phot*[38] package. The photometry was measured using point-spread function (PSF) photometry on the level 2 NIRCam "CAL" images, which preserves the PSF structure compared to level 3 resampled images. The NIRCam pixel area map for the corresponding SW and LW modules must also be applied to each exposure to correct for pixel area variations across the images. Here we use the PSF models provided by WebbPSF (version 1.2.1)[39] to represent the PSF that have been updated to better match the observed PSF in each filter and take into account temporal and spatial variation across the detector. We remove a constant background in the fitting region, which is small enough that a constant background is sufficient. The background is estimated as the median value in an annulus centered at the position with an inner radius of 5 pixels and outer radius of 7 pixels. *space_phot* simultaneously constrains the common flux in all CALs at the forced photometry position within a 5×5 pixel square. The final measured flux is the integral of each full fitted PSF model, which includes a correction to the infinite aperture flux. These total fluxes, which are in units of MJy sr^{-1}, are converted to AB magnitudes using the native pixel scale of each image.

No sources were detected confidently, and we estimate 3σ AB magnitude upper limits of 28.15, 28.31, and 27.90, corresponding to 20.0, 17.3, and 25.2 nJy for the F162M, F356W, and F444W images, respectively. There are three faint source candidates within an arcsecond of the CCO coordinates with signal-to-noise ratio $\approx$ 2–3 in the F162M image. However, these candidate sources are consistent with detector noise patterns seen elsewhere and are not present in other filters, so we judge these to not be credible CCO candidates. We performed the same procedure on a modified version of the F162M image where the so-called $1/f$ noise had been removed by custom processing the stage 2 pipeline output and rerunning the stage 3 pipeline, but this exercise did not yield a deeper limit.

Thus, although our limits are much deeper than those found by Fesen et al. (2006b), as seen in Figure 7, the CCO remains undetected. We should note that even these deep limits are much higher than the expected thermal emission from the NS with $T_{\rm eff} = 2 \times 10^6$ K (e.g., the predicted flux density at 3 μm is $\sim 1.4 \times 10^{-13}$ Jy). However, the measured JWST limits can be used to constrain some possible scenarios in which IR emission could be expected.

First, we can constrain the area of any circular disk with a blackbody temperature similar to the one inferred from the Spitzer detection of the magnetar 4U 0142+61 (Wang et al. 2006). Such a disk with a temperature of $\sim$900 K must have an area smaller than $5.5 \times 10^{20} (\cos i)^{-1}$ cm^2 (i.e., $R_{\rm out} < 0.2 (\cos i)^{-1/2} R_\odot$), where i is the disk inclination and $R_{\rm out}$ is the outer radius of the disk.

The temperature of a realistic fallback disk is expected to decrease outward. If the decrease can be approximated by a power law, $T(r) = T_{\rm in}(r/R_{\rm in})^{-\beta}$, where $T_{\rm in}$ is the temperature at the inner disk radius $R_{\rm in}$, then the spectrum of the disk emission is $f_\nu \propto \nu^{3-(2/\beta)}$ at $kT_{\rm out} \lesssim h\nu \lesssim kT_{\rm in}$, where $T_{\rm out} = T_{\rm in}(R_{\rm in}/R_{\rm out})^\beta$ is the temperature at the outer edge of the disk. For instance, the limiting power-law spectra $f_\nu \propto \nu^{-1}$ and ν^{-2}, shown in Figure 7, correspond to $\beta = 0.5$ and 0.4, respectively.

If the disk is heated by X-rays produced by the NS, one can expect its IR flux to be proportional to the X-ray flux. For Cas A's CCO, the upper limit on the IR-to-X-ray flux ratio is $F_{\rm F356W}/F_{0.6\text{–}6\ \rm keV} < 5 \times 10^{-6}$. This limit is substantially lower than $F_{\rm F356W}/F_{0.6\text{–}6\ \rm keV} \sim 4 \times 10^{-5}$ for the magnetar 4U 0142+61 or $F_{\rm F160W}/F_{\rm X} = 3 \times 10^{-4}$ for the extended NIR emission around the much older ($\sim$0.5 Myr) X-ray thermal isolated NS RX J0806.4−4123 (Posselt et al. 2018).

A power-law spectrum is also expected for nonthermal emission from the NS or from a pulsar wind nebula. In the case of the Cas A CCO, the nonthermal X-ray emission may be faint and overpowered by the strong thermal emission from the NS surface, but nonthermal emission could in principle be detectable at IR wavelengths, where the thermal NS emission

[38] See https://app.soos.io/research/packages/Python/-/space-phot.

[39] https://www.stsci.edu/jwst/science-planning/proposal-planning-toolbox/psf-simulation-tool

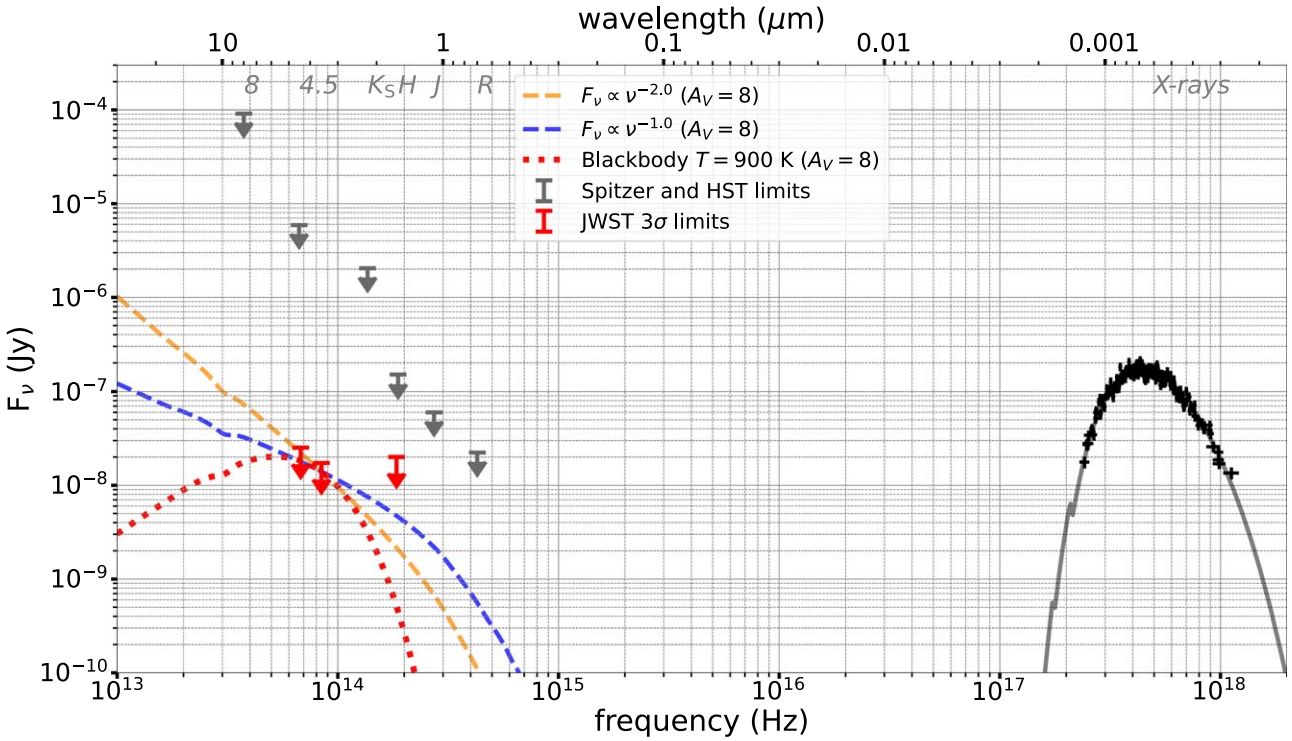

Figure 7. The JWST 3σ upper limits in the NIR (NIRCam F162M, F356W, F444W) at the location of the Cas A CCO and the CCO's X-ray spectrum detected with Chandra ACIS. Power-law spectra consistent with JWST upper limits and an example blackbody spectrum with a temperature of 900 K are plotted for an extinction of $A_V = 8$, using the extinction curve by Gordon et al. (2023). The Chandra ACIS X-ray data are from Posselt & Pavlov (2018), the HST optical and NIR limits are from Fesen et al. (2006b), and the Spitzer limits are from Wang et al. (2007).

is undetectable. The new JWST limits, however, indicate that any nonthermal NS emission must be very faint.

8. Conclusions

We have presented results from an extensive JWST survey of the SNR Cas A made up of NIRCam + MIRI imaging mosaics and exploratory MIRI/IFU spectroscopy. Our observations provide the most detailed and comprehensive mapping ever of its ejecta, CSM/ISM, and associated dust and molecules at NIR and mid-IR wavelengths. Significant findings and implications made from this survey include the following.

1. We have uncovered a weblike network of unshocked ejecta filaments seen in [O IV] emission and resolved to ~0.01 pc scales reflecting turbulent mixing processes and hydrodynamical instabilities that occurred shortly after core collapse of the progenitor star. We weakly detect emission possibly associated with [Fe VIII] 5.446 μm that had been predicted by Laming & Temim (2020) and estimate upward of $\sim 10^{-2}\,M_\odot$ of diffuse, unshocked Fe material. Many aspects of this distribution are relevant for core-collapse SN simulations, including a clear connection seen between the unshocked ejecta filaments and Chandra Fe-K emission. Correlations with NuSTAR are less clear but worth further investigation. This finding is also relevant for attempts to simulate the light curves and spectra of unresolved extragalactic SNe, which must make assumptions regarding the fragmentation of the ejecta due to hydrodynamical instabilities. Ni-bubble expansion reduces the effective optical depth of nonradioactive material (Dessart et al. 2018; Dessart & Audit 2019), and inappropriate treatment could mean that ejecta masses for the majority of stripped-envelope SNe are systematically underestimated (Ergon & Fransson 2022; Ergon et al. 2024).
2. A large structure called the "Green Monster," interior to the main shell and bright in MIRI images, is resolved for the first time. We conclude that this is most likely associated with a thick sheet (or sheets) of dust-dominated emission from shocked CSM seen in projection toward the remnant's interior. The structure is pockmarked with small (~1″) round holes that have most likely been formed by high-velocity N- and He-rich ejecta knots that have pierced through the CSM and driven expanding tangential shocks. Support for this conclusion, including detailed analysis of MIRI/MRS and NIRSpec spectroscopy and correlated X-ray emission observed with Chandra, is provided in De Looze et al. (2024, in preparation) and Vink et al. (2024). The discovery provides an exciting opportunity to probe mass loss of the progenitor system some 10^{4-5} yr prior to explosion.
3. Dozens of light echoes with angular sizes between ~0.″1 and 1′ reflecting previously unseen structure in the ISM are found throughout our NIRCam and MIRI images. Although light echoes had been expected in the vicinity of Cas A, the brightness, the size, and especially the complexity of an echo seen in the southwest corner of our NIRCam mosaics is quite startling. Its fine-scale structure suggests relatively poor mixing and raises questions of how it came to be this way. Is the dust not mixed uniformly into the ISM gas, or is the gas also structured this way? Was this once some sort of concentric shells of outflow from a star that have been buffeted and twisted

by turbulence in the ISM? Are magnetic fields involved? If this structure is typical of the large ISM clouds, do we see the imprint of this on older SNRs in some way? A more detailed investigation of the large southwest echo and other light echoes may start to answer these questions.

4. We do not detect the NS in the center of Cas A. Our NIRCam observations place new upper limits on the CCO's infrared emission ($\lesssim$20 nJy at 3 μm) and tightly constrain scenarios involving a possible fallback disk.

Additional epochs of JWST observations would make it possible to improve the characterization of the kinematic and elemental properties of the ejecta via proper-motion measurements while also permitting further study of nearby light echoes. Imaging mosaics with wider FOVs (reaching 5′ from the center of expansion versus the $\approx$3′ reach of our existing data) would increase opportunities for these measurements dramatically and cover the northeast/southwest outflows to more accurately constrain their total mass, composition, and relationship to the original SN (Fesen & Milisavljevic 2016). Additional spectroscopy, including wide-field NIRSpec microshutter assembly observations across the entire SNR and targeted MIRI/MRS observations of regions interior to the main shell (especially ones that overlap with ^{44}Ti emission), would be invaluable to improve estimates of chemical abundances and place the deepest limits possible for the total Fe yield.

Acknowledgments

This work is based on observations made with the NASA/ESA/CSA James Webb Space Telescope. The data were obtained from the Mikulski Archive for Space Telescopes at the Space Telescope Science Institute, which is operated by the Association of Universities for Research in Astronomy, Inc., under NASA contract NAS 5-03127 for JWST. These observations are associated with program No. 1947. Support for program No. 1947 was provided by NASA through a grant from the Space Telescope Science Institute, which is operated by the Association of Universities for Research in Astronomy, Inc., under NASA contract NAS 5-03127.

This research was supported by the Munich Institute for Astro-, Particle and BioPhysics (MIAPbP), which is funded by the Deutsche Forschungsgemeinschaft (DFG; German Research Foundation) under Germany's Excellence Strategy —EXC-2094—390783311. We are grateful for the Lorentz Center for hosting the workshop "Supernova Remnants in Complex Environments," where some ideas used in this manuscript were developed. Tracey DeLaney provided Spitzer IRS and VLA *S*-band data that were inspected as part of this paper. Brian Grefenstette provided the NuSTAR ^{44}Ti map used in this paper. Una Hwang provided the Chandra 1 Ms image used in this paper. D.M. is grateful for conversations with Luc Dessart, who contributed ideas used in this paper. D.M. acknowledges invaluable support from Mark Linvill and Chris Orr, who help manage the computational resources used to complete this research.

D.M. acknowledges NSF support from grants PHY-2209451 and AST-2206532. T.T. acknowledges support from NSF grant 2205314 and JWST grant JWST-GO-01947.031. J.M.L. was supported by JWST grant JWST-GO-01947.023 and by basic research funds of the Office of Naval Research. I.D.L. acknowledges funding from the Belgian Science Policy Office (BELSPO) through the PRODEX project "JWST/MIRI Science exploitation" (C4000142239). I.D.L., F.K., and N.S. S. have received funding from the European Research Council (ERC) under the European Union's Horizon 2020 research and innovation program DustOrigin (ERC-2019-StG-851622). M.J. B. acknowledges support from the ERC grant SNDUST ERC-2015-AdG-694520. M.M. and R.W. acknowledge support from an STFC Consolidated grant (ST/W000830/1). S.O. acknowledges support from PRIN MUR 2022 (20224MNC5A). B.-C. K. acknowledges support from the Basic Science Research Program through the NRF of Korea funded by the Ministry of Science, ICT and Future Planning (RS-2023-00277370). Work by R.G.A. was supported by NASA under award No. 80GSFC21M0002. The research of J.C.W. is supported by NSF AST-1813825. H.-T.J. is grateful for support from the German Research Foundation (DFG) through the Collaborative Research Centre "Neutrinos and Dark Matter in Astro- and Particle Physics (NDM)," grant No. SFB-1258-283604770, and under Germany's Excellence Strategy through the Cluster of Excellence ORIGINS EXC-2094-390783311.

Facilities: JWST(MIRI), JWST(NIRCam).

Appendix

The color composite images shown in the body of this paper are for showing the relative differences between multiple filters of data, but they can also hide details that are present within the individual data sets, especially for our MIRI imaging. As indicated in Figure 2, some bandpasses are dominated by continuum emission, and others contain both continuum and line emission. In Figures A1, A2, and A3 of this appendix, we show images of each filter of the NIRCam and MIRI imaging mosaics individually to allow these details to be assessed on a filter-by-filter basis.

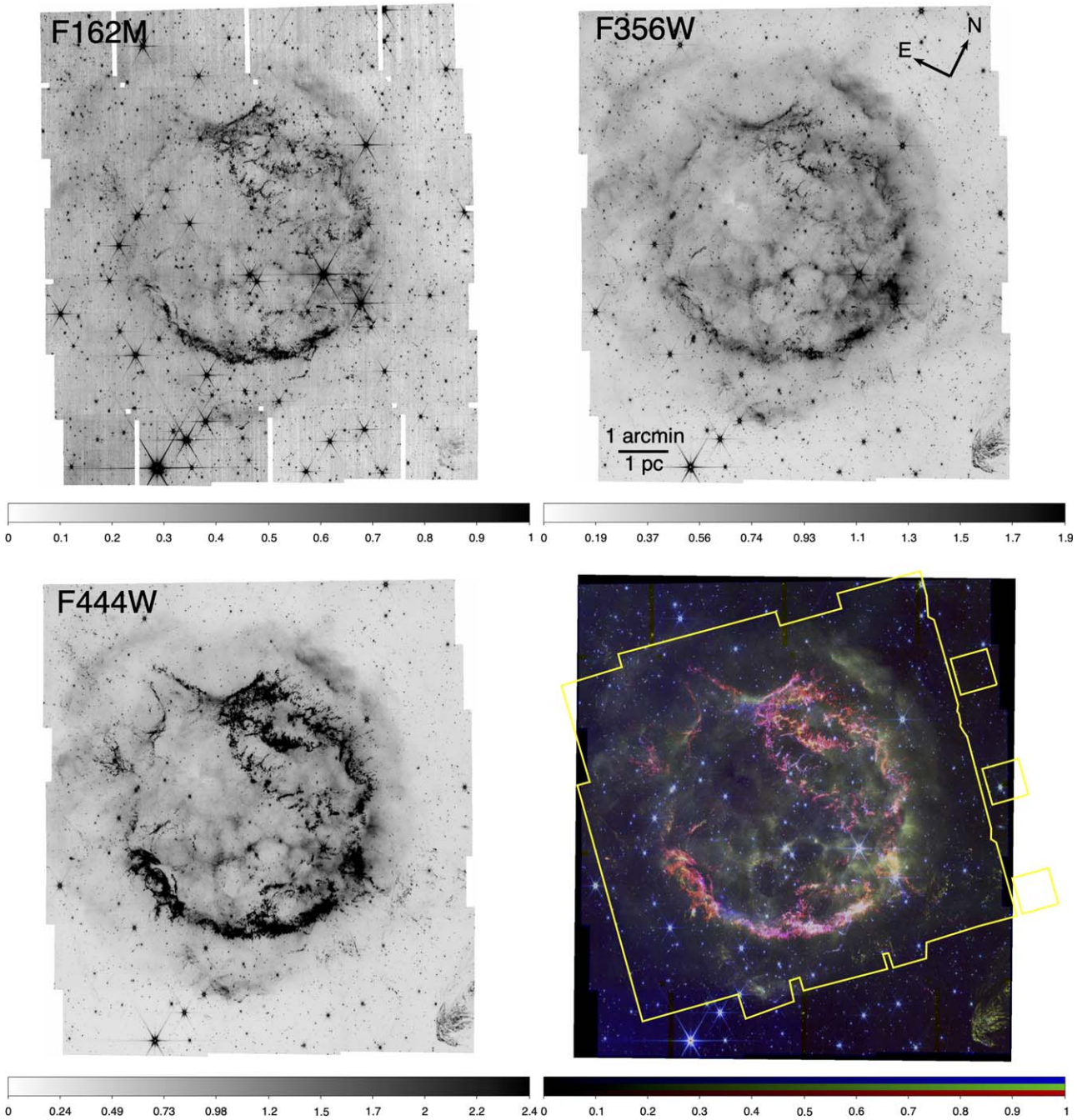

Figure A1. Three NIRCam imaging mosaics obtained as part of our Cas A survey. The F162M filter was used as the SW channel for both the F356W and F444W observations, so the exposure time is twice as long. Gaps are seen in the F162M mosaic because of the dithering three-point pattern that prioritized the LW filters and introduced gaps in the SW channel detectors. The images have the same angular scale and orientation, and the intensity scale is in units of MJy sr^{-1}. In the color version at lower right, the blue, green, and red show the images in increasing wavelength, respectively. The approximate footprint of the MIRI mosaics is shown.

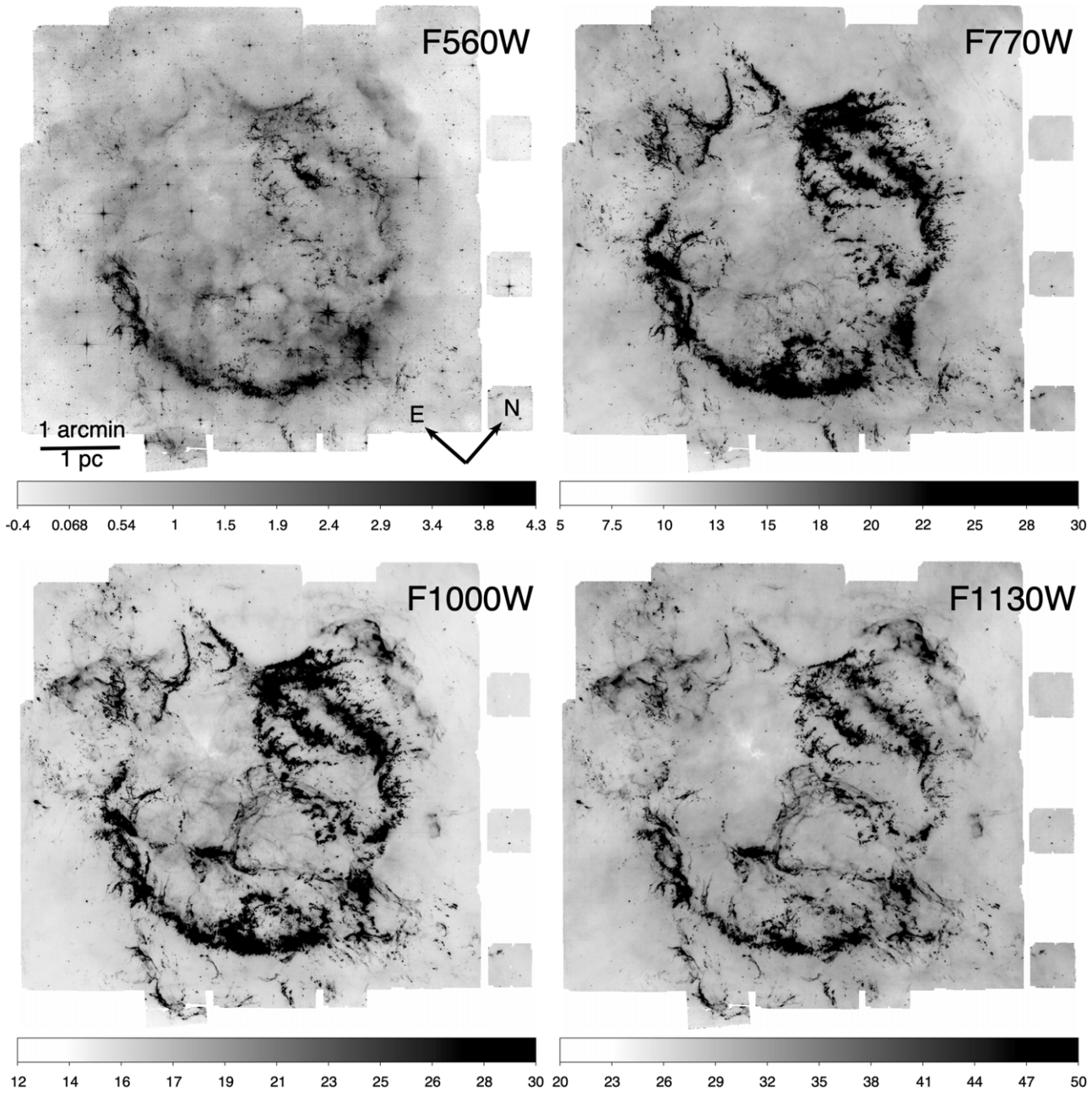

Figure A2. The four shorter-wavelength MIRI imaging mosaics obtained as part of the survey. The full spatial coverage (including the Lyot coronagraph) is shown. The common angular scale and orientation are shown in the upper left panel. Color bars depict the intensity scale that has units of MJy sr^{-1}.

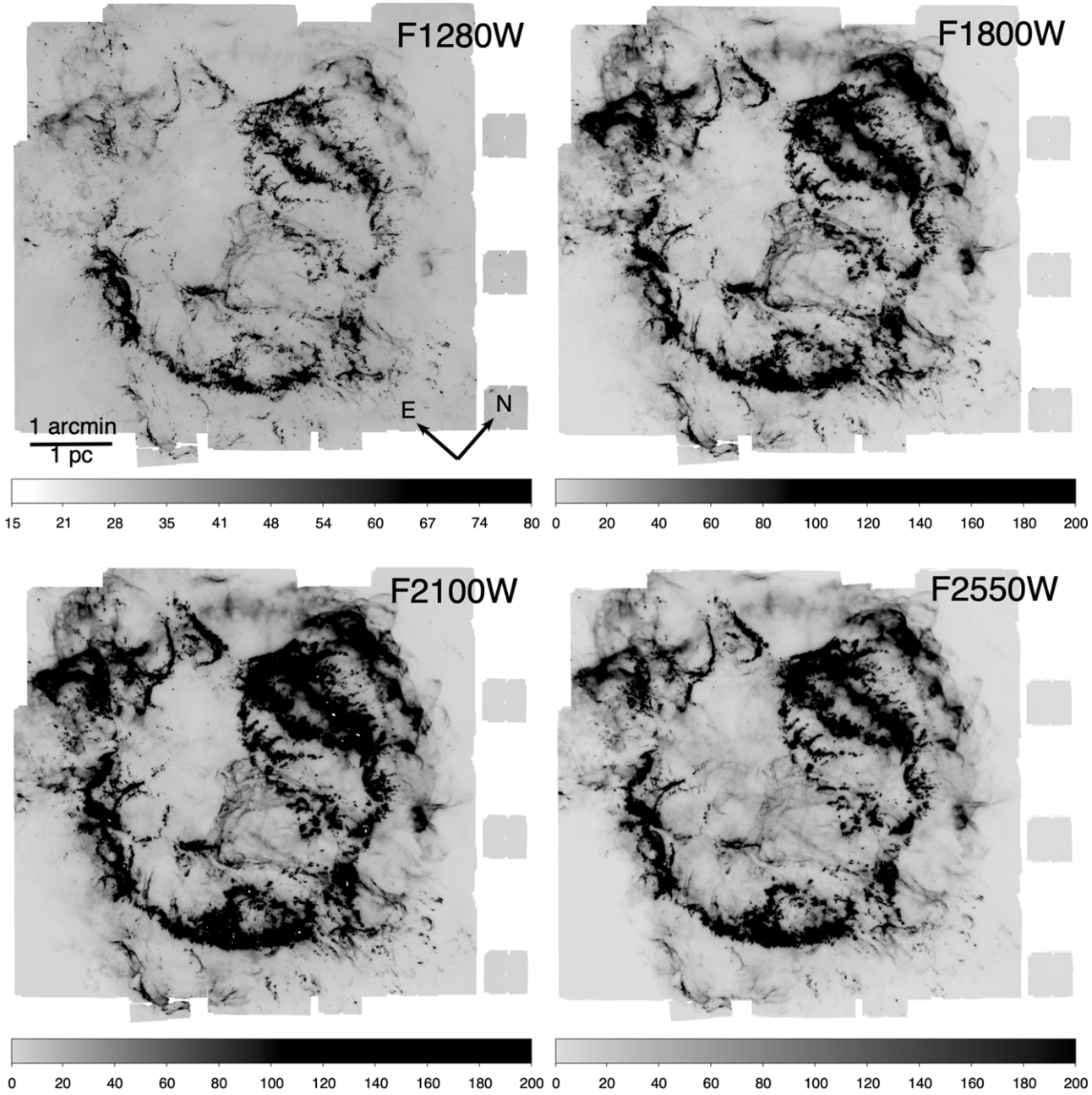

Figure A3. Same as Figure A2 except showing the four longer-wavelength MIRI imaging mosaics.

ORCID iDs

Dan Milisavljevic https://orcid.org/0000-0002-0763-3885
Tea Temim https://orcid.org/0000-0001-7380-3144
Ilse De Looze https://orcid.org/0000-0001-9419-6355
Danielle Dickinson https://orcid.org/0000-0003-0913-4120
J. Martin Laming https://orcid.org/0000-0002-3362-7040
Robert Fesen https://orcid.org/0000-0003-3829-2056
John C. Raymond https://orcid.org/0000-0002-7868-1622
Richard G. Arendt https://orcid.org/0000-0001-8403-8548
Jacco Vink https://orcid.org/0000-0002-4708-4219
Bettina Posselt https://orcid.org/0000-0003-2317-9747
George G. Pavlov https://orcid.org/0000-0002-7481-5259
Ori D. Fox https://orcid.org/0000-0003-2238-1572
Ethan Pinarski https://orcid.org/0009-0003-5244-3700
Bhagya Subrayan https://orcid.org/0000-0001-8073-8731
Judy Schmidt https://orcid.org/0000-0002-2617-5517
William P. Blair https://orcid.org/0000-0003-2379-6518
Armin Rest https://orcid.org/0000-0002-4410-5387
Daniel Patnaude https://orcid.org/0000-0002-7507-8115
Bon-Chul Koo https://orcid.org/0000-0002-2755-1879
Jeonghee Rho https://orcid.org/0000-0003-3643-839X
Salvatore Orlando https://orcid.org/0000-0003-2836-540X
Hans-Thomas Janka https://orcid.org/0000-0002-0831-3330
Michael J. Barlow https://orcid.org/0000-0002-3875-1171
Adam Burrows https://orcid.org/0000-0002-3099-5024
Roger Chevalier https://orcid.org/0000-0002-9117-7244
Geoffrey Clayton https://orcid.org/0000-0002-0141-7436
Claes Fransson https://orcid.org/0000-0001-8532-3594
Christopher Fryer https://orcid.org/0000-0003-2624-0056
Haley L. Gomez https://orcid.org/0000-0003-3398-0052

Florian Kirchschlager https://orcid.org/0000-0002-3036-0184
Jae-Joon Lee https://orcid.org/0000-0003-0894-7824
Mikako Matsuura https://orcid.org/0000-0002-5529-5593
Justin D. R. Pierel https://orcid.org/0000-0002-2361-7201
Felix D. Priestley https://orcid.org/0000-0002-5858-6265
Aravind P. Ravi https://orcid.org/0000-0002-7352-7845
Nina S. Sartorio https://orcid.org/0000-0003-2138-5192
Melissa Shahbandeh https://orcid.org/0000-0002-9301-5302
Patrick Slane https://orcid.org/0000-0002-6986-6756
Nathan Smith https://orcid.org/0000-0001-5510-2424
Kathryn Weil https://orcid.org/0000-0002-8360-0831
Roger Wesson https://orcid.org/0000-0002-4000-4394
J. Craig Wheeler https://orcid.org/0000-0003-1349-6538

References

Al Kharusi, S., BenZvi, S. Y., Bobowski, J. S., et al. 2021, NJPh, 23, 031201
Alarie, A., Bilodeau, A., & Drissen, L. 2014, MNRAS, 441, 2996
Alford, J. A. J., & Halpern, J. P. 2023, ApJ, 944, 36
Andresen, H., Müller, B., Müller, E., & Janka, H.-T. 2017, MNRAS, 468, 2032
Arendt, R. G., Dwek, E., Kober, G., Rho, J., & Hwang, U. 2014, ApJ, 786, 55
Argyriou, I., Glasse, A., Law, D. R., et al. 2023, A&A, 675, A111
Arias, M., Vink, J., de Gasperin, F., et al. 2018, A&A, 612, A110
Baars, J. W. M., Genzel, R., Pauliny-Toth, I. I. K., & Witzel, A. 1977, A&A, 61, 99
Barlow, M. J., Krause, O., Swinyard, B. M., et al. 2010, A&A, 518, L138
Bellm, E. C., Kulkarni, S. R., Graham, M. J., et al. 2019, PASP, 131, 018002
Besel, M. A., & Krause, O. 2012, A&A, 541, L3
Bianchi, S., & Schneider, R. 2007, MNRAS, 378, 973
Biscaro, C., & Cherchneff, I. 2016, A&A, 589, A132
Blasi, P. 2013, A&ARv, 21, 70
Blondin, J. M., Borkowski, K. J., & Reynolds, S. P. 2001, ApJ, 557, 782
Blondin, J. M., & Ellison, D. C. 2001, ApJ, 560, 244
Bocchio, M., Marassi, S., Schneider, R., et al. 2016, A&A, 587, A157
Burrows, A., Radice, D., Vartanyan, D., et al. 2020, MNRAS, 491, 2715
Burrows, A., & Vartanyan, D. 2021, Natur, 589, 29
Bushouse, H., Eisenhamer, J., Dencheva, N., et al. 2022, JWST Calibration Pipeline, v1.8.2, Zenodo, doi:10.5281/zenodo.7229890
Chevalier, R. A., & Kirshner, R. P. 1978, ApJ, 219, 931
Chevalier, R. A., & Oishi, J. 2003, ApJL, 593, L23
Couch, S. M., Wheeler, J. C., & Milosavljević, M. 2009, ApJ, 696, 953
Dalla Vecchia, C., & Schaye, J. 2008, MNRAS, 387, 1431
De Looze, I., Barlow, M. J., Swinyard, B. M., et al. 2017, MNRAS, 465, 3309
De Luca, A. 2017, JPhCS, 932, 012006
DeLaney, T., Kassim, N. E., Rudnick, L., & Perley, R. A. 2014, ApJ, 785, 7
DeLaney, T., & Rudnick, L. 2003, ApJ, 589, 818
DeLaney, T., Rudnick, L., Stage, M. D., et al. 2010, ApJ, 725, 2038
Dessart, L., & Audit, E. 2019, A&A, 629, A17
Dessart, L., Hillier, D. J., & Wilk, K. D. 2018, A&A, 619, A30
Domček, V., Vink, J., Hernández Santisteban, J. V., DeLaney, T., & Zhou, P. 2021, MNRAS, 502, 1026
Dwek, E. 1998, ApJ, 501, 643
Dwek, E., & Arendt, R. G. 2008, ApJ, 685, 976
Eldridge, J. J., Fraser, M., Smartt, S. J., Maund, J. R., & Crockett, R. M. 2013, MNRAS, 436, 774
Eldridge, J. J., Izzard, R. G., & Tout, C. A. 2008, MNRAS, 384, 1109
Ellinger, C. I., Rockefeller, G., Fryer, C. L., Young, P. A., & Park, S. 2013, arXiv:1305.4137
Ellinger, C. I., Young, P. A., Fryer, C. L., & Rockefeller, G. 2012, ApJ, 755, 160
Ennis, J. A., Rudnick, L., Reach, W. T., et al. 2006, ApJ, 652, 376
Ergon, M., & Fransson, C. 2022, A&A, 666, A104
Ergon, M., Lundqvist, P., Fransson, C., et al. 2024, A&A, 683, A241
Eriksen, K. A., Arnett, D., McCarthy, D. W., & Young, P. 2009, ApJ, 697, 29
Fesen, R. A. 2001, ApJS, 133, 161
Fesen, R. A., & Gunderson, K. S. 1996, ApJ, 470, 967
Fesen, R. A., Hammell, M. C., Morse, J., et al. 2006a, ApJ, 645, 283
Fesen, R. A., & Milisavljevic, D. 2016, ApJ, 818, 17
Fesen, R. A., Morse, J. A., Chevalier, R. A., et al. 2001, AJ, 122, 2644
Fesen, R. A., Pavlov, G. G., & Sanwal, D. 2006b, ApJ, 636, 848
Fesen, R. A., Winkler, F., Rathore, Y., et al. 1997, AJ, 113, 767
Fryer, C. L., Burns, E., Hungerford, A., et al. 2023, ApJ, 956, 19
Gardner, J. P., Mather, J. C., Abbott, R., et al. 2023, PASP, 135, 068001
Ginzburg, V. L., & Syrovatskii, S. I. 1965, ARA&A, 3, 297
Gordon, K. D., Clayton, G. C., Decleir, M., et al. 2023, ApJ, 950, 86
Gotthelf, E. V., Halpern, J. P., & Alford, J. 2013, ApJ, 765, 58
Grefenstette, B. W., Fryer, C. L., Harrison, F. A., et al. 2017, ApJ, 834, 19
Grefenstette, B. W., Harrison, F. A., Boggs, S. E., et al. 2014, Natur, 506, 339
Halpern, J. P., & Gotthelf, E. V. 2010, ApJ, 709, 436
Hirata, K., Kajita, T., Koshiba, M., Nakahata, M., & Oyama, Y. 1987, PhRvL, 58, 1490
Hoyle, F., & Wickramasinghe, N. C. 1970, Natur, 226, 62
Hughes, J. P., Rakowski, C. E., Burrows, D. N., & Slane, P. O. 2000, ApJL, 528, L109
Hungerford, A. L., Fryer, C. L., & Rockefeller, G. 2005, ApJ, 635, 487
Hungerford, A. L., Fryer, C. L., & Warren, M. S. 2003, ApJ, 594, 390
Hurford, A. P., & Fesen, R. A. 1996, ApJ, 469, 246
Hwang, U., & Laming, J. M. 2012, ApJ, 746, 130
Hwang, U., Laming, J. M., Badenes, C., et al. 2004, ApJL, 615, L117
Isensee, K., Rudnick, L., DeLaney, T., et al. 2010, ApJ, 725, 2059
Ivezić, Ž., Kahn, S. M., Tyson, J. A., et al. 2019, ApJ, 873, 111
Jakobsen, P., Ferruit, P., Alves de Oliveira, C., et al. 2022, A&A, 661, A80
Janka, H.-T. 2012, ARNPS, 62, 407
Janka, H.-T., Melson, T., & Summa, A. 2016, ARNPS, 66, 341
JDADF Developers, Averbukh, J., Bradley, L., et al. 2023, Jdaviz, v3.7.1, Zenodo, doi:10.5281/zenodo.10041721
Jiang, B. W., Zhang, K., & Li, A. 2005, ApJL, 630, L77
Jones, T. J., Rudnick, L., DeLaney, T., & Bowden, J. 2003, ApJ, 587, 227
Kerzendorf, W. E., Do, T., de Mink, S. E., et al. 2019, A&A, 623, A34
Khokhlov, A. M., Höflich, P. A., Oran, E. S., et al. 1999, ApJL, 524, L107
Kim, Y., Rieke, G. H., Krause, O., et al. 2008, ApJ, 678, 287
Kirchschlager, F., Schmidt, F. D., Barlow, M. J., De Looze, I., & Sartorio, N. S. 2023, MNRAS, 520, 5042
Kirchschlager, F., Schmidt, F. D., Barlow, M. J., et al. 2019, MNRAS, 489, 4465
Kochanek, C. S. 2018, MNRAS, 473, 1633
Koo, B.-C., Kim, D., Yoon, S.-C., & Raymond, J. C. 2023, ApJ, 945, 158
Koo, B.-C., Kim, H.-J., Lee, Y.-H., et al. 2018, ApJ, 866, 139
Koo, B.-C., Kim, H.-J., Oh, H., et al. 2020, NatAs, 4, 584
Koo, B.-C., & Park, C. 2017, in Handbook of Supernovae, ed. A. W. Alsabti & P. Murdin (Berlin: Springer), 161
Krause, O., Birkmann, S. M., Usuda, T., et al. 2008, Sci, 320, 1195
Krause, O., Rieke, G. H., Birkmann, S. M., et al. 2005, Sci, 308, 1604
Kushnir, D., & Katz, B. 2015, ApJ, 811, 97
Laming, J. M., Hwang, U., Radics, B., Lekli, G., & Takács, E. 2006, ApJ, 644, 260
Laming, J. M., & Temim, T. 2020, ApJ, 904, 115
Lawrence, S. S., MacAlpine, G. M., Uomoto, A., et al. 1995, AJ, 109, 2635
Lee, J.-J., Park, S., Hughes, J. P., & Slane, P. O. 2014, ApJ, 789, 7
Lee, Y.-H., Koo, B.-C., Moon, D.-S., Burton, M. G., & Lee, J.-J. 2017, ApJ, 837, 118
Maeda, K., & Nomoto, K. 2003, ApJ, 598, 1163
Mandal, S., Duffell, P. C., Polin, A., & Milisavljevic, D. 2023, ApJ, 956, 130
Maund, J. R., Smartt, S. J., Kudritzki, R. P., Podsiadlowski, P., & Gilmore, G. F. 2004, Natur, 427, 129
Milisavljevic, D., & Fesen, R. A. 2013, ApJ, 772, 134
Milisavljevic, D., & Fesen, R. A. 2015, Sci, 347, 526
Milisavljevic, D., & Fesen, R. A. 2017, in The Supernova—Supernova Remnant Connection, ed. A. W. Alsabti & P. Murdin (Berlin: Springer), 2211
Morse, J. A., Fesen, R. A., Chevalier, R. A., et al. 2004, ApJ, 614, 727
Murphy, J. W., Ott, C. D., & Burrows, A. 2009, ApJ, 707, 1173
Nelson, D., Pillepich, A., Springel, V., et al. 2019, MNRAS, 490, 3234
Nittler, L. R., & Ciesla, F. 2016, ARA&A, 54, 53
Nomoto, K., Kobayashi, C., & Tominaga, N. 2013, ARA&A, 51, 457
Ono, M., Nagataki, S., Ferrand, G., et al. 2020, ApJ, 888, 111
Orlando, S., Miceli, M., Pumo, M. L., & Bocchino, F. 2016, ApJ, 822, 22
Orlando, S., Ono, M., Nagataki, S., et al. 2020, A&A, 636, A22
Orlando, S., Wongwathanarat, A., Janka, H. T., et al. 2021, A&A, 645, A66
Orlando, S., Wongwathanarat, A., Janka, H. T., et al. 2022, A&A, 666, A2
Ouyed, R., Leahy, D., Ouyed, A., & Jaikumar, P. 2011, PhRvL, 107, 151103
Patnaude, D. J., & Fesen, R. A. 2009, ApJ, 697, 535
Pavlov, G. G., & Luna, G. J. M. 2009, ApJ, 703, 910
Pavlov, G. G., Sanwal, D., & Teter, M. A. 2004, in Young Neutron Stars and Their Environments, ed. F. Camilo & B. M. Gaensler, Vol. 218 (San Francisco, CA: ASP), 239
Pavlov, G. G., Zavlin, V. E., Aschenbach, B., Trümper, J., & Sanwal, D. 2000, ApJL, 531, L53

Posselt, B., & Pavlov, G. G. 2018, ApJ, 864, 135
Posselt, B., Pavlov, G. G., Ertan, Ü., et al. 2018, ApJ, 865, 1
Posselt, B., & Pavlov, G. G. 2022, ApJ, 932, 83
Powell, J., & Müller, B. 2019, MNRAS, 487, 1178
Priestley, F. D., Arias, M., Barlow, M. J., & De Looze, I. 2021, MNRAS, 509, 3163
Priestley, F. D., Barlow, M. J., & De Looze, I. 2019, MNRAS, 485, 440
Reber, G. 1944, ApJ, 100, 279
Reed, J. E., Hester, J. J., Fabian, A. C., & Winkler, P. F. 1995, ApJ, 440, 706
Rest, A., Foley, R. J., Sinnott, B., et al. 2011, ApJ, 732, 3
Rest, A., Pierel, J., Correnti, M., et al. 2023, arminrest/jhat: The JWST HST Alignment Tool (JHAT), v2, Zenodo, doi:10.5281/zenodo.7892935
Rest, A., Suntzeff, N. B., Olsen, K., et al. 2005, Natur, 438, 1132
Rest, A., Welch, D. L., Suntzeff, N. B., et al. 2008, ApJL, 681, L81
Rho, J., Gomez, H. L., Boogert, A., et al. 2018, MNRAS, 479, 5101
Rho, J., Kozasa, T., Reach, W. T., et al. 2008, ApJ, 673, 271
Rho, J., Park, S.-H., Arendt, R., et al. 2024, ApJL, submitted
Rho, J., Reach, W. T., Tappe, A., et al. 2009, in ASP Conf. Ser. 414, Cosmic Dust—Near and Far, ed. T. Henning, E. Grün, & J. Steinacker (San Francisco, CA: ASP), 22
Rho, J., Reynolds, S. P., Reach, W. T., et al. 2003, ApJ, 592, 299
Rieke, M. J., Kelly, D. M., Misselt, K., et al. 2023, PASP, 135, 028001
Rosenberg, I. 1970, MNRAS, 147, 215
Ryder, S. D., Van Dyk, S. D., Fox, O. D., et al. 2018, ApJ, 856, 83
Sato, T., Maeda, K., Nagataki, S., et al. 2021, Natur, 592, 537
Sato, T., Yoshida, T., Umeda, H., et al. 2020, ApJ, 893, 49
Shternin, P. S., Ofengeim, D. D., Heinke, C. O., & Ho, W. C. G. 2023, MNRAS, 518, 2775
Sieverding, A., Kresse, D., & Janka, H.-T. 2023, ApJL, 957, L25
Slavin, J. D., Dwek, E., Mac Low, M.-M., & Hill, A. S. 2020, ApJ, 902, 135
Smartt, S. J. 2009, ARA&A, 47, 63
Smith, N. 2014, ARA&A, 52, 487
Smith, N., Silverman, J. M., Chornock, R., et al. 2009, ApJ, 695, 1334
Soker, N. 2018, arXiv:1805.03447
Szczepańczyk, M. J., Antelis, J. M., Benjamin, M., et al. 2021, PhRvD, 104, 102002
Tananbaum, H. 1999, IAUC, 7246, 1
Temim, T., Slane, P., Reynolds, S. P., Raymond, J. C., & Borkowski, K. J. 2010, ApJ, 710, 309
Thorstensen, J. R., Fesen, R. A., & van den Bergh, S. 2001, AJ, 122, 297
Tonry, J. L., Denneau, L., Heinze, A. N., et al. 2018, PASP, 130, 064505
Uchiyama, Y., & Aharonian, F. A. 2008, ApJL, 677, L105
van den Bergh, S. 1965, PASP, 77, 269
van den Bergh, S. 1971, ApJ, 165, 457
Vance, G. S., Young, P. A., Fryer, C. L., & Ellinger, C. I. 2020, ApJ, 895, 82
Vartanyan, D., Burrows, A., Wang, T., Coleman, M. S. B., & White, C. J. 2023, PhRvD, 107, 103015
Viganò, D., & Pons, J. A. 2012, MNRAS, 425, 2487
Vink, J. 2004, NewAR, 48, 61
Vink, J., Agarwal, M., Slane, P., et al. 2024, ApJL, 964, L11
Vink, J., & Laming, J. M. 2003, ApJ, 584, 758
Vogelsberger, M., Genel, S., Springel, V., et al. 2014, MNRAS, 444, 1518
Vogt, F. P. A., Besel, M.-A., Krause, O., & Dullemond, C. P. 2012, ApJ, 750, 155
Wang, Z., Chakrabarty, D., & Kaplan, D. L. 2006, Natur, 440, 772
Wang, Z., Kaplan, D. L., & Chakrabarty, D. 2007, ApJ, 655, 261
Williams, B. J., & Temim, T. 2017, in Handbook of Supernovae, ed. A. W. Alsabti & P. Murdin (Berlin: Springer), 2105
Wongwathanarat, A., Janka, H. T., & Müller, E. 2013, A&A, 552, A126
Wongwathanarat, A., Janka, H.-T., Müller, E., Pllumbi, E., & Wanajo, S. 2017, ApJ, 842, 13
Wongwathanarat, A., Müller, E., & Janka, H.-T. 2015, A&A, 577, A48
Woosley, S. E., Heger, A., & Weaver, T. A. 2002, RvMP, 74, 1015
Wright, G. S., Rieke, G. H., Glasse, A., et al. 2023, PASP, 135, 048003
Young, P. A., Fryer, C. L., Hungerford, A., et al. 2006, ApJ, 640, 891